THESIS FOR THE DEGREE OF DOCTOR OF PHILOSOPHY

Emerging Mechanisms of FeCrAl(RE) oxide scale formation and permeation from 1st principles

VEDAD BABIĆ

Department of Chemistry and Chemical Engineering
CHALMERS UNIVERSITY OF TECHNOLOGY
Göteborg, Sweden 2019.

Emerging Mechanisms of FeCrAl(RE) oxide scale formation and permeation from 1st principles

VEDAD BABIĆ
ISBN 978-91-7597-877-2

Doktorsavhandlingar vid Chalmers Tekniska Högskola
Ny serie nr 4558
ISSN 0346-718X
Department of Chemistry and Chemical Engineering
Chalmers University of Technology
SE-412 96 Göteborg
Sweden
Telephone: +46 (0)31-772 1000

Chalmers Reproservice
Göteborg, Sweden 2019.

Emerging Mechanisms of FeCrAl(RE) oxide scale formation and permeation from 1st principles

Thesis for the degree of Doctor of Philosophy

VEDAD BABIĆ
Department of Chemistry and Chemical Engineering
Chalmers University of Technology

Abstract

Alumina forming alloys are important for high temperature applications due to the high stability of the α-Al_2O_3 scale which forms above 900°C. FeCrAl(RE) alloys are alumina formers with small additions of reactive elements, RE e.g. Y, Zr, Hf and Ce, added to improve among others oxidation behavior and scale adhesion. Cr is added to the binary FeAl system in the role of a 3rd element in order to decrease early Fe, and internal Al oxidation, and promote α-Al_2O_3 formation. As corrosion and oxidation processes deplete the alloy of scale forming metal alloy, the durability suffers. Here, density functional theory, DFT has been employed to study parameters controlling oxide scale growth in general and permeation of oxidants through formed scales on FeCrAl(RE) in particular.

The context of oxide growth is given by Wagner theory of oxidation in which diffusion of ionic species; cations, anions, and electrons control oxide growth rate. Inasmuch as alumina is a large band-gap insulator, the conduction band is inaccessible for electron transport. Thus, electron transport utilizing oxygen vacancies has been studied here. Activation energies for electron transport were calculated to be $\sim$ 0.5 eV rendering electrons mobile. Oxygen vacancy, V_O diffusion barriers range between $\sim$2-5 eV depending on electronic charge of the vacancy. A percolative V_O and electron transport is thus proposed in alumina, rendering both species mobile.

The third element effect was given a local meaning at early stages of scale growth in a systematic study comparing Sc, Ti, V, Cr, Mn, Fe, Co, and Ni employed as guest ions in an alumina lattice. Comparing the affinity to oxygen vacancies, V_O only Cr and V displayed ideal intermediate affinities, i.e. intermediate to Fe and Al. V was thus proposed alongside Cr as a third element in the Fe-TM-Al ternary alloy system.

Chromia nodules embedded in the protective alumina scale formed on FeCrAl(RE) were observed to permeate nitrogen in a reducing 95% N_2, 5% H_2, 35 ppm H_2O environment. Al in the alloy was shown to reduce the chromia particle upon which a nitrogen permeation channel through said particle is sustained and for which Al acts as nitrogen sink.

Enhanced oxidation was observed around surface RE-oxide particles. Here, oxidation of Al by water is understood to be the driving force for incorporating RE into alumina grain-boundaries. This RE decoration retards grains coarsening, leading to a thicker and more adherent early scale. In O_2 containing atmospheres, this defect rich "messy" scale eventually becomes oxidized, upon which hydride ions are consumed and RE precipitate. RE(III) are shown to introduce stresses into grain-boundaries leading to a faster precipitation while smaller RE(IV) can maintain enhanced oxidation for longer before precipitation occurs.

Keywords: DFT, oxidation, alumina, reactive elements, nitridation, hydrogen, water

Acknowledgements

First and foremost, I would to acknowledge my supervisors, Itai and Torbjörn for their great help and tutoring during my PhD studies. Itai, it has been a privilege to have you as my main supervisor and it is a great inspiration to see how tirelessly and with great joy you work with science. Torbjörn, although we have not always discussed my work in great theoretical depths, I always appreciated how you forced me to consider the bigger picture, and how my results fit within it. I would also like to thank Christine for our fruitful collaborations, discussions and for providing context to my work.

Jan-Erik, Lars-Gunnar and Ulf, I thank you for all the help and support you have provided when needed. Our administrators and economists, Sandra, Susanne, Anna, and Christina, thank you for all the help and assistance with administrative matters.

Valentina, my theoretical chemistry colleague, thank you for helping me whenever I needed help, especially with the super computers.

I'm grateful to my office mates, Julien and Robin, with whom I had many coffees and conversations, probably the most, unless I had more together with Patrik, in case of which I am still grateful. Additionally I would like to thank all my current and former colleagues at Environmental Inorganic Chemistry in the Division of Energy and Materials for creating a great working atmosphere.

I would like to acknowledge the High Temperature Corrosion center (HTC) for the collaboration and discussions resulting in the published papers. Moreover, I would like to acknowledge Chalmers Centre for Computational Science and Engineering (C3SE) for providing computing resources.

A big thanks to Marlene, thank you for being supportive of me and my undertakings, always, and giving me advice whenever I ask for it. I'm looking forward to spend many years together with you. I'm dearly thankful to my parents who taught me the value of education, and encouraged its pursuit. You have showed me how to be selfless and help others without expecting anything in return, which I greatly appreciate. I'm thankful to my sister, her family and my brother for being there for me whenever I need someone to talk to.

List of publications

This thesis consists of an extended summary and the following appended papers:

Paper I **Transition metal attenuated mechanism for protective alumina formation from first principles**
V. Babic, C. Geers and I. Panas, RSC Adv., 8, 41255 (2018).

Paper II **Properties of Alumina/Chromia Scales in N_2-Containing Low Oxygen Activity Environment Investigated by Experiment and Theory**
C. Geers, V. Babic, N. Mortazavi, M. Halvarsson, B. Jönsson, L.G. Johansson, I. Panas and J.E. Svensson, Oxid. Met., 87(3-4), 321-332 (2017)

Paper III **Fates of Hydrogen During Alumina Growth Below Yttria Nodules in FeCrAl(RE) at Low Partial Pressures of Water**
V. Babic, C. Geers, and I. Panas, Electrocat., 8(6), 565-576 (2017)

Paper IV **Interplay of water and reactive elements in oxidation of alumina-forming alloys**
N. Mortazavi, C. Geers, M. Esmaily, V. Babic, M. Sattari, K. Lindgren, P. Malmberg, B. Jönsson, M. Halvarsson, J.E. Svensson, I. Panas and L.G. Johansson, Nat. Mat., 17, 610-617 (2018)

Paper V **Reactive element effects in high temperature alloys disentangled**
V. Babic, C. Geers, and I. Panas, Comm. Chem. (Submitted)

Statement of Author's Contribution

I The author performed all calculations and wrote the article together with co-authors.

II The author performed all DFT calculations and contributed to the writing of the computational parts.

III The author performed all DFT calculations and contributed to the writing of the computational parts.

IV The author performed most calculations, contributed to the writing of section 9 "Modeling considerations and computational details" in the supplementary information and to the interpretation of results.

V The author performed all calculations and wrote the article together with co-authors.

Contents

Part I
Introduction

1 Background

From small screws, construction materials to components in power plants, fuel cells and engines, metals are everywhere around us. What they all share is that they are subject to corrosion, the degradation of a metal by its environment. The cost of corrosion has been estimated to be $297b in the USA (1998) (*1*) and $310b in China (2014) (*2*) owing to environmental, process reliability and safety issues. It thus becomes natural to strive to reduce the impact of corrosion to achieve a sustainable society.

Corrosion is mitigated by e.g. the ability of alloys to form a protective oxide scale suitable for the considered application. While an alloy may show good corrosion resistance at ambient conditions, it may fail at elevated temperatures, thus it must be optimized for both gaseous environment and temperature. Stainless steels, for example, contain chromium which forms a chromia scale instead of a rapidly growing iron or nickel oxide making it suitable for applications up to several hundred degrees Celsius, but this chromia scale is susceptible to processes which deplete the Cr-content e.g. Cr-evaporation (*3*). Instead, at these temperatures, alumina forming alloys such as FeCrAl(RE) can be used as the formed α-Al_2O_3 scale offers more protection (*4*). FeCrAl(RE) applications include heating elements and components in high temperature furnaces, and they are even considered as components for nuclear power generation such as fuel cladding owing to their high corrosion resistance (*5*, *6*). These iron based alloys often contain nominally between 3-6 wt.% Al and 5-15% wt. Cr with small amounts of reactive elements (RE, e.g. Y, Zr, and Hf) which have shown to improve among others oxidation properties (*7*–*9*). Chromium is added to the Fe-Al system as a third element in that chromium promotes α-alumina formation and decreases iron oxidation (*10*, *11*). The most common type of failure in these alloys is the depletion of aluminium which prevents the reformation of α-alumina and allows for the formation of faster growing oxides, so called break-away oxidation (*12*).

The context of the present theoretical work is given by experiments performed on a FeCrAl(RE) alloy in both oxidizing, 100% O_2 (containing impurity ppm H_2O) and reducing, 95% N_2/5% H_2/ 35 ppm H_2O environments at 900°C, in order to understand alloy behavior in both extremes. The formation of chromia and alumina in are both environments thermodynamically stable and the alloy forms a thin protective α-alumina scale with chromia nodules and reactive element (RE) particles scattered across the surface.

In O_2-containing environments, alumina growth is controlled by the cathodic reduction of oxygen at the scale/gas interface and the inwards diffusion of oxygen anions but the ionic transport mechanism is still unclear (*13*) and has lead to the coining of the "corundum conundrum" (*14*) (Sec. 2.6). In reducing environments, water, the role of which has been a long-standing issue (*13*, *15*), acts as the single oxidant. Inasmuch as alumina is a large band-gap insulator, electron transport is difficult and water is transported neutrally as

hydroxides in grain-boundaries. This inwards transport continues until an inner cathode is reached. Here, hydroxide hydrogen is reduced owing to electron transfer from the nominal anode at the alloy/scale interface where generic defects comprising oxygen vacancies are formed. Under reducing conditions, these become occupied by either O^{2-} or H^{+} forming hydrides $H^{-}@V_O$, both of water origin. The accommodation of hydride ions in the oxide renders the alumina scale defect rich.

Interestingly, nitrogen which is considered to be chemically inert towards reactions with chromia or alumina, is observed to form various metal nitrides (AlN, CrN, Cr_2N) beneath an apparently protective alumina scale containing micron sized chromia inclusions. Thus, the alloy becomes depleted of free Al, detrimental for the ability of the alloy to continuously support the reformation of a protective alumina scale.

Enhanced oxidation is observed around RE oxide particles in which Al-oxidation by water catalyzes RE decoration of alumina interfaces and grain-boundaries. The instantaneous RE oxide decoration of grain-boundaries disallows alumina grains to coarsen and keeps them open as transport channels. This effect is observed in both dry O_2 and reducing environments, with the difference that in O_2 environments, oxygen eventually oxidizes deposited reduced species such as hydride ions in the transient defective alumina scale leading to RE oxide precipitation and grains coarsening, whereby α-Al_2O_3 is formed. This understanding emerging from the present work is detailed in Fig. 1.1.

This mechanistic insight has been achieved by analyzing corrosion processes on a fundamental level and how they impact the formation and degradation of protective oxide scales in order to create new materials with improved durability. The underlying processes involved in high temperature oxidation are mainly transport controlled; cation, anion, and electron transport of which all are necessary to explicitly take into account when studying new materials and their oxides. With increased computational capacity and improved methodology, it becomes possible to study more and more complex chemical systems on an atomistic scale by first-principle calculations to arrive at novel insights feeding into future alloy development efforts. Thus, density functional theory, DFT was in this work employed to study

(i) oxygen vacancy and electron transport in α-Al_2O_3, a large band-gap insulator and the effect transition metals, TM (Sc, Ti, V, Cr, Mn, Fe, Co, Ni) have on these, especially in early stage growth and how it relates to the third element effect (Paper I)

(ii) why nitridation only occurs beneath chromia scales and how nitrogen is transported through the chromia scale (Paper II and III)

(iii) the fate of hydrogen at hydroxylated alumina interfaces when water acts as main oxidant (Paper III and IV)

(iv) a water mediated RE (Sc, Ti, Y, Zr, Hf, La, Ce) decoration of alumina interfaces, where REs keep interfaces open to increase aluminum oxidation until the RE precipitate (Papers IV and V)

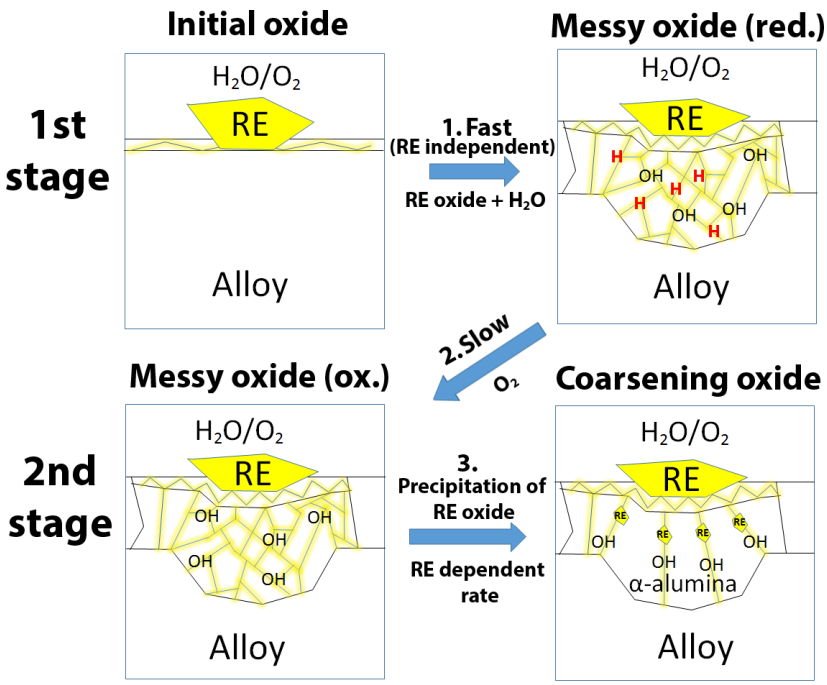

Figure 1.1: Reactive element assisted scale formation disentangled: 1. Fast formation of a nano-granular messy oxide owing to aluminum oxidation by water. RE oxide assisting in scale permeation of water in the form of H^+ and OH^- results in RE ions co-decoration of alumina grain-boundary interfaces, irrespective of RE oxide. Residual hydrogen, being accumulated as hydride ions in charged oxygen vacancies, renders the messy oxide partially reduced. 2. Partially reduced messy oxide, upon being oxidized by O_2, renders the resulting RE decorated aluminum oxy-hydroxide unstable. 3. RE dependent rate of precipitation, RE(III) faster than RE(IV), controls the rate of grains coarsening.

2 High Temperature Oxidation

Corrosion resistance and long-term mechanical durability (strength, creep) are necessary to ensure the usefulness of high-temperature alloys over time. The degradation occurs through various corrosive and mechanical stress processes often involving so-called break-away oxidation. Interestingly, oxidation offers a main means to resist corrosion, i.e. by forming a dense, well adherent, slowly growing oxide scale which protects the underlying metal from further rapid oxidation. In alumina forming, FeCrAl alloys at high temperatures, this protective oxide scale is α-Al_2O_3 (corundum), the thermodynamically most stable aluminum-oxide. It is usually observed to form above 900 °C (*8*) but has been reported to form at temperatures as low as 700 °C (*16*). Alumina growth on FeCrAl alloys at high temperatures (>900 °C) is dominated by short-circuit diffusion (*17*, *18*) with a mixed outwards and inwards oxide growth (*19*). The most common type of failure in these alloys is the depletion of aluminum by e.g. internal oxidation, which prevents the re-formation of the α-Al_2O_3 scale leading to the oxidation of other alloying elements, mainly Fe, which do not offer protection against oxygen uptake, leading to a linear mass gain - "break-away oxidation" (*12*). The oxide growth can be tuned by varying the contents of the different alloying elements.

Additions of Cr to the binary FeAl alloy promotes the formation of a defect free protective alumina scale by reducing Fe oxidation in an effect called the third element effect. Also, Cr is observed to reduce internal oxidation of Al in the alloy matrix. This is an additional manifestation of the fact chromium oxidation is fast, and while kinetics favors formation of Cr_2O_3 thermodynamics favors α-Al_2O_3 formation. Finally, structural similarities between the two oxides also facilitates the formation of the latter (*10*, *11*).

A fourth class of elements is often added to the alumina formers, comprising the so called reactive elements, RE e.g. Zr, Y, La, Ce (*7–9*, *20–22*). In alumina formers, several effects have been reported of which three are (i) improved scale adherence, (ii) a change from mixed out/inwards growing oxide to a mainly inwards-growing oxide, (iii) and a change in the scale morphology (*8*, *9*, *21*). It has been found necessary (but not sufficient) for the RE to segregate to grain-boundaries in order to provide a positive effect on the oxidation resistance . Along this line, it has also been proposed that the ion size needs to be large enough in order to induce a steric effect which inhibits cation outwards diffusion (*9*). Having said this, an additional RE effect is associated with acting sinks for sulphur that else is known to segregate to the alloy/scale interface and cause spalling (*7*, *9*).

The conceptual framework of the presented work is offered by Wagner's electrochemical theory of oxidation. Here, the oxidation process is realized by electron transfer from a nominal anode at the alloy/scale interface to scale surface. This electron transfer renders the two interfaces charged, resulting in an outwards diffusion of cations and inwards diffusion of anions in order to neutralize the two interfaces. Moreover, local thermodynamic equilibrium is assumed to be established at every point throughout the scale. Ultimately, Wagner theory can be applied to make macroscopic predictions of the overall oxidation kinetics, and has found success in describing the oxide growth of e.g. CoO (*23*).

Thus, during initial stages of FeCrAl(RE) oxidation, the oxide is understood to nucleate

on metal surfaces and grow laterally until a thin film is formed. The resulting mixed (Fe,Cr,Al) oxide is transformed according to order of thermodynamic stability of the corresponding oxides. The introduction of RE suppresses outwards diffusion of cations leaving inwards oxygen transport as the dominant mobile ionic scale forming species. In this context, it follows from Wagner theory of oxidation that oxide scale growth requires the existence of both oxygen ions and electron transport channels across the scale in order to able to reduce O_2(g) while maintaining charge neutrality. Often, electron mobility is assumed to be non-rate-limiting, leaving the rate of scale growth to be determined by oxygen vacancy diffusion. The diffusivity, D is determined by Arrhenius equation:

$$D = D_0 exp(-\frac{E_A}{RT}) \tag{2.1}$$

Where E_A is the activation energy for diffusion and D_0 a maximal diffusion coefficient. Thus by studying the activation energy for diffusion, we may gain insight into what controls the diffusivity during formation of the oxide scale. Inasmuch as alumina growth on FeCrAl(RE) alloys becomes dominated by inwards diffusion of oxygen, the growth rate is understood to be determined by (i) non-electrochemical correlated RE and water transport to access the effective "inner" cathode and (ii) a coupled oxygen vacancy and electron transport to support the actual oxidation process. This allows for the generalization of the Wagnerian understanding to include the diffusion of species into the oxide scale prior to being reduced at the (inner) cathode.

Indeed, in this work conventional Wagner theory is found to be sufficient in explaining internal Al nitridation in FeCrAl. This is contrasted by the oxidation of FeCrAl(RE) by water being transported as hydroxides to the inner cathode where the hydroxide hydrogen become reduced.

In order to make contact between this conceptual understanding and the reality it claims to describe, where macroscopic kinetics studies are coupled with powerful microscopic techniques, a complementary atomistic perspective is provided here by 1st principles modelling. Elemental distribution, morphology, texture, grain size, oxide composition and inhomogeneity, all constitute boundary conditions that ensure the relevance of the atomistic studies.

In what follows, after a short detour into basic thermodynamics, some mathematical realizations of oxide scaling kinetics are presented followed by discussions concerning design of atomistic models, all in order to illustrate the usefulness of this Wagnerian paradigm.

2.1 Thermodynamics

Thermodynamics is the study of heat and temperature and their relation to energy and work. It is said to have developed in the early 19^{th} century in order to improve the accuracy of steam engines by among others the "father of thermodynamics" Sadi Carnot. Although first applied to engines, it was quickly adopted into chemistry by J.W. Gibbs in what is sometimes called chemical thermodynamics, the study of heat and work in

chemical reactions. Consider the following general metal oxidation reaction:

$$xM(s) + \frac{y}{2}O_2(g) \rightarrow M_xO_y \tag{2.2}$$

Whether this reaction is spontaneous or not depends on if the free energy of the products are lower than those of the reactants. This is often expressed as a change in Gibbs' free energy i.e. if it's positive, the reaction is non-spontaneous and if negative it is spontaneous:

$$\Delta G = \sum \Delta G_{products} - \sum \Delta G_{reactants} \tag{2.3}$$

where G is a function of enthalpy H, temperature T, and entropy S:

$$G = H - TS = U + PV - TS \tag{2.4}$$

The enthalpy of a system is the sum of its internal energy, U and the product of its pressure, P and volume, V. Since the internal energy is not measurable, only changes in Gibbs' free energy become relevant. In systems at constant temperature and pressure, a common experimental environment, the change in Gibbs' free energy becomes:

$$\Delta G = \Delta H - T\Delta S = \Delta U - T\Delta S \tag{2.5}$$

Note that the calculated reaction energies by quantum chemical tools such as DFT (see Ch. 3) are taken to be the change in internal energy. As the calculations are performed in vacuum there is no displacement of matter by the formation of the materials and the calculated energy becomes enthalpy.

Entropy, S is often explained as disorder or chaos and may be expressed in different ways depending on the type of chemical reaction that occurs. Configurational entropy is related to the number of available (equivalent) configurations in which the system may reside. An example would be surface adsorption of a molecule where all available adsorption sites form the configurational space, Ω:

$$S_{\text{conf}} = k_B ln(\Omega) \tag{2.6}$$

where k_B is the Boltzmann constant. It is very important to note that configurational entropy only comes into play at equilibrium or when there is sufficient time to actually visit all possible configurations. It does not come into play in e.g. quick diffusion processes where the diffusing species does not have sufficient time to visit all available states.

Other contributions are arrived at if the degrees of freedom change between products and reactants e.g. adsorption reactions, where translational degrees of freedom are lost.

As the reader will notice, there have been no calculated configurational entropy contributions in the appended papers due to this reason. The entropic contribution arising from a change in degrees of freedom has been calculated where necessary e.g. adsorption or gas evolution reactions.

2.1.1 Stability of Oxides

In order to compare the thermodynamic stability of oxides, the Gibb's energy can also be expressed as a function of temperature, T, the gas constant, R and the reaction quotient,

Q_r:

$$\Delta G = \Delta G^0 + RTlnQ_r \tag{2.7}$$

$$Q_r = \frac{a(M_xO_y)}{a(M)^x a(O_2)^{\frac{y}{2}}}|_t \tag{2.8}$$

where Q_r is a product of activities at time t before equilibrium has been established and is related to the equilibrium constant by taking Q_r at infinite time, $K_{eq} = Q_r|_{t=\infty}$. At equilibrium, $\Delta G = 0$:

$$\Delta G^0 = -RTlnK_{eq} = -RTln\frac{a(M_xO_y)}{a(M)^x a(O_2)^{\frac{y}{2}}} \tag{2.9}$$

In an ideal case, following Raoult's law, the activity of a solid is assumed to be identity while the activity of a gas is assumed to be it's partial vapor pressure p_i. Applied to eq. (2.2), the Gibb's free energy is estimated to be

$$\Delta G^0 = -RTln(p_{O_2}) \tag{2.10}$$

Given a known ΔG^0, the lowest partial pressure of oxygen at which the oxide is stable, the dissociation pressure, can be calculated by solving eq. (2.10) for p_{O_2};

$$p_{O_2} = exp(-\frac{\Delta G^0}{RT}) \tag{2.11}$$

It is then possible to compare the relative stabilities of oxides at a chosen temperature in an Ellingham diagram (ΔG^0 plotted against T).

2.2 Oxidation Kinetics

Depending on the scale formed, and the environment under which the oxide grows, various types of growth kinetics are observed. The overall kinetics are studied by either measuring oxide thickness or mass gain as function of time. This technique, although good at capturing the overall oxidation behavior, fails at capturing local phenomena e.g. secondary oxidant contributions such as internal nitridation which require more advanced analysis using e.g. electron microscopy. Fig. 2.1 illustrates a few selected oxidation kinetics.

2.2.1 Parabolic Oxide Growth

The earliest report of parabolic oxide growth found in recent literature are the papers of T.G Tammann (1920), and Pilling and Bedworth (1923), who reported that oxide growth is ruled by a parabolic rate law. Tammann showed this as a relationship between oxide growth rate and inverse oxide thickness:

$$\frac{dx}{dt} = k_p\frac{1}{x} \tag{2.12}$$

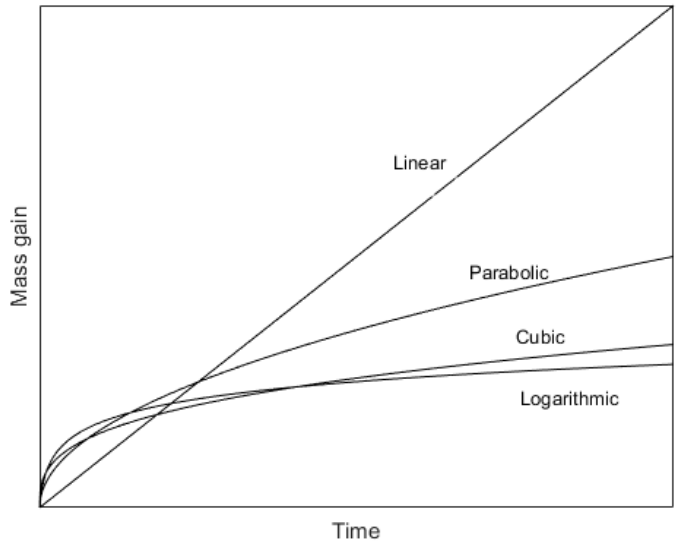

Figure 2.1: Mass gain curves illustrating linear, parabolic, logarithmic and cubic kinetics.

where x is the oxide layer thickness and k_p a parabolic rate constant. Pilling and Bedworth showed the same rate law using a mass gain formalism:

$$(\frac{\Delta m}{A})^2 = k_p t \tag{2.13}$$

where Δm is the mass gained during oxidation and A is the surface area of the metal. Both Tammann, and Pilling and Bedworth wrongly assumed the diffusion of neutral species and it would take 13 years until Carl Wagner's 1933 paper (*24*) in which the parabolic rate law is derived mathematically by assuming the diffusion of ionic species; anions, cations and electrons, citing both Tammann, and Pilling and Bedworth for their experimental contributions in demonstrating parabolic growth.

2.2.2 Sub-parabolic Oxide Growth

Sub-parabolic kinetics are associated with an initially quicker oxide growth rate (compared to parabolic) which later drops off. Thus a thick early transient oxide is formed which transforms to a protective α-alumina. This is discussed in Paper I and Sec. 4.1 and connects to the third element effect. Two sub-parabolic oxidation kinetics are covered here, logarithmic and the for alumina growth at high temperatures more common, cubic growth rate (*25*).

Logarithmic Oxidation Kinetics.

Logarithmic mass gain is typically obtained at lower temperatures and in thin oxides where electrons can tunnel through the oxide scale. An electric field is established across the thin scale which drives the diffusion process of charged species. This is also called Cabrera-Mott kinetics (*26*, *27*) defined as:

$$\Delta m = k \ln(t + t_0) + C \tag{2.14}$$

where k and C are constants. As the scale grows and the tunneling path closes, other kinetics are obtained. It may also be derived by assuming that the ionic diffusion barrier, W is scale thickness dependent:

$$W = W_0 + \mu x \tag{2.15}$$

where μ is a constant characteristic of the oxide. As the oxide grows, the activation energy increases leading to a decreased diffusivity. The growth rate becomes:

$$\frac{dx}{dt} = c \times exp[\frac{-(W_0 + \mu x)}{kT}] \tag{2.16}$$

which integrates to a logarithmic function:

$$x = A \times ln(1 + Bt) \tag{2.17}$$

Similarily, when oxide growth is coupled to grains coarsening by adding a quadratic term to the activation energy, quasi-logarithmic kinetics are obtained (think of a spring force which resists parabolic scale growth) (*28*):

$$W = W_0 + \mu x^2 \tag{2.18}$$

$$\frac{dx}{dt} = c \times exp[\frac{-(W_0 + \mu x^2)}{kT}] \tag{2.19}$$

which for small times behaves parabolically and as t increases approaches the (square root) logarithmic limit. The integrated equation becomes:

$$x = A \times \sqrt{ln(1 + Bt)} \tag{2.20}$$

Cubic Oxidation Kinetics

It is important to note that during the oxidation process, not only is the oxide thickening, but often the grains also grow in size with thickness. The effective grain-boundary density is then reduced and the earlier mentioned parabolic growth becomes sub-parabolic (cubic) (*25*):

$$\Delta m^3 = k_c t \tag{2.21}$$

where k_c is a cubic oxide rate constant.

2.2.3 Breakaway Oxidation

Breakaway oxidation or chemical failure is a term used to denote different types of failure during the oxidation process. Considering that the alloy is continuously being depleted of scale forming element, a critical point may be reached when formation of a non-protective oxide scale becomes thermodynamically favored. This type of breakaway behavior is referred to as intrinsic chemical failure. Additionally, scale spalling and cracking may lead to mechanically induced chemical failure (MICF) (*29*). Having said this, the main cause of failure in FeCrAl alloys is the depletion of free Al, thus initiating break-away oxidation (*12*). The resulting growth of iron-rich oxides displays a linear mass gain:

$$\Delta m = kt \tag{2.22}$$

This type of kinetics is obtained under conditions where diffusion of species through the scale is not rate limiting e.g. where surface processes limit the oxidation rate (*30*).

2.3 Modelling Considerations for Transport in Alumina on FeCrAl(RE)

Conventional Wagner theory required both electron and ion diffusion for scale growth. The large band gap in alumina renders the conduction band inaccessible. Rather impurity states in the band gap are required for electron transport. Generic such states comprise the very same oxygen vacancies that are responsible for the inwards growth of alumina on FeCrAl(RE). Charge of oxygen vacancy as well as any adjacent redox active aliovalent cation in the alumina lattice are expected to affect the oxygen vacancy mobility.

2.3.1 Oxygen Vacancy Diffusion

Thus, oxygen vacancy diffusion was studied by calculating activation barriers of diffusion in an alumina lattice. The models employed are based on a 2×2×1 supercell of α-Al_2O_3 in which one Al-atom is substituted for a transition metal, TM (Sc, Ti, V, Cr, Mn, Fe, Co, Ni) and an oxygen vacancy is formed by deleting one O-atom. Two structures, one "Start" and one "End" structure, are formed by removing the O-atom at two different, but neighboring sites. Both structures are relaxed while keeping the lattice parameters fixed. A full Linear Synchronous Transit/Quadratic Synchronous Transit (LST/QST) search scheme is employed to find the transition state between the two structures, see Ref. (*31*). The input is a simple linear interpolation between the two structures and an example using ten images is shown in Fig. 2.2.

2.3.2 Electron Transport

There are two relevant frameworks which have been developed to study electron transfer, Marcus theory and small polaron hopping theory. Marcus theory was initially developed to study electron transfer reactions in solutions, but later extended to include solids. Small polaron theory on the other hand is based on polaronic trapping of charge carriers

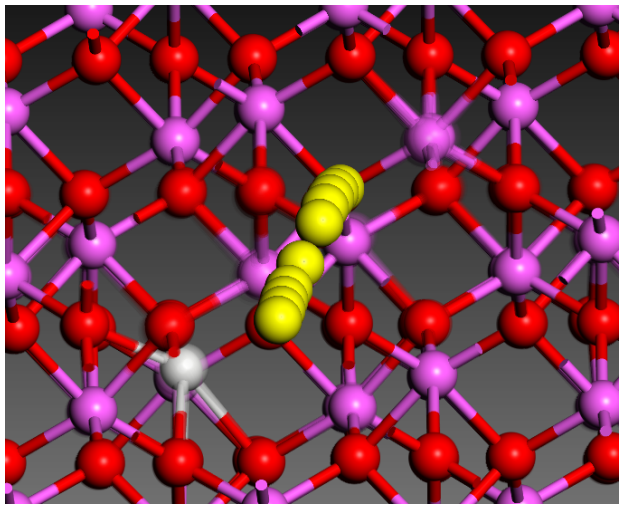

Figure 2.2: Example of a ten image linear interpolation between start (vacancy next to transition metal) and end structures in an oxygen vacancy diffusion process which goes as input to a first LST saddle point search. Red - oxygen, purple - Al, gray - Sc, yellow - diffusing oxygen atom.

in solids. At a first glance they might seem quite different but in their application to electron transfer in alumina they become equivalent.

Polarons refer to carriers (electrons/holes) which introduce lattice relaxations, deforming the original lattice structure thus stabilizing the carrier into a bound state. The polarons are therefore also considered to be "self-trapped". Examples include e.g. Fe reduction where the $Fe^{3+} \rightarrow Fe^{2+}$ reaction introduces relaxations around the Fe ion stabilizing the reduced ion state or more relevant to this work, where lattice relaxations stabilize electrons in oxygen vacancies. Small polarons are thus those in which the relaxations are considered small, either located to a single lattice site or restricted to a single unit cell.

Marcus theory is based on the possibility of calculating free energy curves, $\Psi_i(q)$ for the two species involved in the electron transfer reaction, see Fig. 2.4. Relevant parameters become activation energy, ΔE^*, reaction energy ΔE^0. Other parameters include reorganization energy, λ_i and the electronic coupling constant w_{AB}. Note though that the calculated activation energy is the energy required to relax the structure as to allow electron tunneling, the potential barrier which is tunneled through is not calculated here.

Thermal fluctuations in nuclear coordinates allow the system to reach the transition state at $q = X_{AB}$. Although Marcus does not discuss polarons, it is obvious that the various relaxed states of reactants and products are polaronic in nature. With DFT, it is straightforward to approximate free energy curves employing a LST scheme. In Fig. 2.3 a five image linear interpolation has been superposed to visualize the geometrical relaxations when a vacancy becomes charged from Q=0→2+, whose energies define the

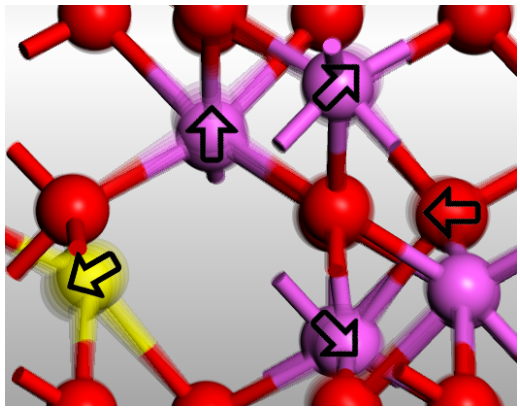

Figure 2.3: A five image linear interpolation superposed with arrows visualizing the geometrical polaronic relaxations associated with doubly charging a neutral vacancy. Red - oxygen, purple - Al, yellow - Sc.

free energy surface of $C^{**} \rightarrow C$. The reactant and product states are chosen such that A (B) is the combined system before (after) electron transfer.

$$C^* + D \rightarrow C + D^* \tag{2.23}$$

where C and D are any atoms or molecules which can donate or accept electrons and the star (*) denotes electron which is being transferred. Ψ_A then correspond to the free energy curve of system $C^* + D$ and Ψ_B is then simply that of $C + D^*$. Elsewhere, Marcus theory is used to calculate rate constants for electron transfer reactions, which has not been applied here.

2.4 Modelling Considerations for Internal Nitridation of FeCrAl(RE)

Internal nitridation in reducing environments was observed and reported in Paper II beneath chromia nodules on the surface of a FeCrAl(RE) alloy. It becomes important to understand why and how chromia, unlike alumina and yttria permeates nitrogen. Inasmuch as alumina is more thermodynamically stable than chromia, we understand Al in the alloy to continuously reduce the Cr_2O_3 scale, by which a Wagnerian flow of oxygen vacancies is maintained through the oxide scale. This continuous reduction facilitates N_2 dissociation and promotes N^{3-} transport through the chromia scale in oxygen vacancies by the formation of transient chromium oxy-nitrides. Thus, aluminum is understood as acting sink for nitrogen in the form of AlN and oxygen as α-Al_2O_3.

Throughout, viable paths for nitrogen absorption are sought. (I) As oxide grains have varying orientations and their surface terminations are ill defined generic conditions for N_2 sticking and dissociation were addressed. The employed models were thus taken to be the simplest possible i.e. O_x-M-O-...-M-O_{1-x} stacked layers, allowing for a variation in

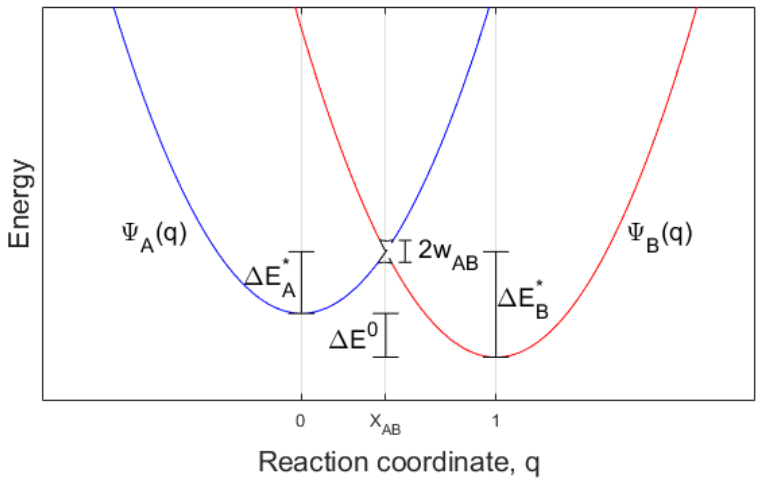

Figure 2.4: Free energy curve vs reaction coordinate for an electron transfer reaction. Ψ_A is the free energy curve of the initial configuration and Ψ_B the free energy curve for the configuration after electron transfer. X_{AB} is the crossing between the two along the reaction coordinate q. ΔE_i^* is the activation energy of the electron transfer between configurations i =A,B, and ΔE^0 refers to the relative stability of A and B. The electronic coupling constant, w_{AB}, is neglected in our study.

surface oxygen termination, by moving oxygen atoms from one surface to the other, while maintaining nominal oxide stoichiometries. (II) The transient chromium oxy-nitrides were constructed by substituting oxygen for nitrogen whereby one oxygen vacancy is introduced for every two nitrogen ions in a chromia lattice with corundum structure.

2.5 Modelling Considerations for FeCrAl(RE) Oxidation by Water

Paper III concerns the fate of hydrogen in a reducing environment where 35 ppm of water acts as single oxidant. Inasmuch as alumina is a large band-gap insulator, cathode reduction of water on the scale surface becomes virtually inaccessible. Instead water permeates the scale as hydroxides into the oxide until an inner cathode is reached. Oxygen vacancies, formed at the scale/alloy interface supply electrons to the cathode. Outwards diffusion of said vacancies results in them eventually being occupied by either hydroxide oxygen ($O^{2-}@V_O$) or hydrogen ($H^-@V_O$). This oxidation process is quasi-Wagnerian, i.e. no (surface) cathode reduction is involved. Rather, the inner cathode is accessed by Fickian diffusion along hydroxylated grain-boundaries. Subsequently, a correlated RE and water mechanism for FeCrAl(Y) oxidation is addressed in Papers IV and V. The oxidation of aluminum at the scale/alloy interface is understood to be the driving force for incorporating RE-oxide as "water equivalents" e.g. $Y_{2/3}O$ (Paper IV), and more generally

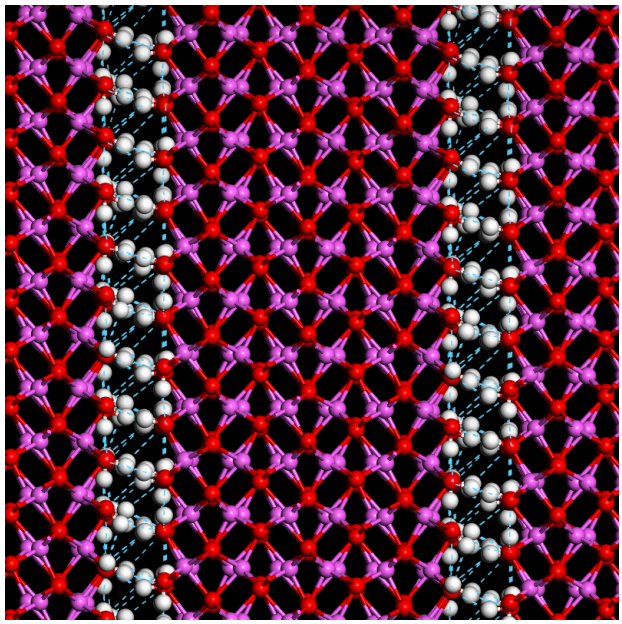

Figure 2.5: Hydroxylated interface model between 1.5 nm thick α-alumina lamella. Color code: Al – purple, O – red, H – white, light blue dashed lines denote hydrogen bonds.

$RE(III)_{2/3}O$ and $RE(IV)_{1/2}O$ (Paper V) in alumina interfaces in low water environments.

The hydroxylated grain-boundary model is constructed by allowing the fusion of hydroxylated 0001 surfaces of alumina slabs, see Fig. 2.5 offering intermediate in the effective redox processes, including also oxy-hydroxy-hydride transients. This hydroxylated interface model is taken as a starting point for the RE/hydroxide co-decoration mechanism, modelled by substitutionally doping the interface with Y (Paper IV). In Paper V, a possible generalization of the findings for Y(III) to include Sc(III), Y(III), La(III); Ti(IV), Zr(IV), Hf(IV), and Ce(III)/Ce(IV) was attempted. Depending on oxidation state, RE(III) or RE(IV), three or four H-atoms per RE were removed, allowing for the study of water-mediated RE decoration of alumina interfaces during scale growth.

2.6 The Corundum Conundrum

As grain-boundary diffusion is the dominant ion transport path at high temperatures in alumina it has been thought to offer a lower activation energy (25-40%) (*20*) compared to lattice diffusion. Measurements on the other hand report a higher activation energy for grain-boundary diffusion (*32*). It is important to note that activation energy measurements on alumina were performed on sintered and spontaneously formed alumina scales and that these differ from thermally growing oxides. The defect structure of the latter is maintained by the mechanisms involved in oxide growth, absent in the former cases (*32*). First principle calculations of activation energies were reported to be around 2 eV

while measurements give 5-6 eV. This is the so called "**corundum conundrum**" (*14*, *33*). While some studies have tried to reconcile the measured experimental values with calculations (*34*, *35*), we instead maintain that the measured values may not be valid for thermally grown oxides, and instead propose a coupled oxygen vacancy/electron hopping mechanism to resolve the conundrum, see Sec. 4.1.

3 Quantum Chemistry

Quantum chemistry is the reformulation of quantum mechanics to address problems in chemistry. As all classical objects in classical physics obey Newtonian mechanics do quantum objects obey quantum mechanics. The quantum world makes its presence known in our everyday life, in sunlight, in energy conversion, and quantum mechanics explains the structure of the periodic table of the elements. Fundamental knowledge of the quantum world can be made accessible by interrogating the wavefunction that results from solving the so-called Schrödinger equation (*36*). Being able to formulate this fundamental equation in principle, the next problem is how? Indeed, due to its complexity, the solutions to the Schrödinger equation for real systems are inaccessible directly, that is with one exception, the hydrogen atom. Instead, ingenious reformulations and corresponding computational methods have been developed. In the following paragraphs the predominant reformulation of the Schrödinger equation - that is Density Functional Theory DFT - is outlined in conjunction with central computational methods that become relevant in DFT.

3.1 The Schrödinger Equation

The general, time-dependent Schrödinger equation describes how a quantum mechanical state, $\psi(x,t)$ evolves in time, and is postulated to be (for a one-particle, one-dimensional system):

$$i\hbar\frac{\partial\psi(x,t)}{\partial t} = -\frac{\hbar^2}{2m}\frac{\partial^2\psi(x,t)}{\partial x^2} + V(x,t)\psi(x,t) \tag{3.1}$$

where $\hbar$ is the reduced Planck's constant, $V(x,t)$ is the potential-energy function of the system and m is the mass of the particle. Not many quantum mechanical applications use this form of the Schrödinger equation. Instead it is the simpler, time-independent form which is used. It is derived by assuming that the potential-energy function, $V(x,t)$ has no time-dependence i.e. a system in equilibrium. The time-independent form of Eq. 3.1 is found by variable separation, $\psi(x,t) = \psi(x)f(t)$. Rearranging the equation so that each hand-side only contains one of the variables, and setting them equal to a constant E, the equation becomes:

$$-\frac{\hbar^2}{2m}\frac{d^2\psi(x)}{dx^2} + V(x)\psi(x) = E\psi(x) \tag{3.2}$$

where E is postulated to be the energy of the system. This equation can be expressed as

$$\hat{H}\psi(x) = E\psi(x) \tag{3.3}$$

where $\hat{H}$ is the Hamiltonian, an operator containing all interactions acting within the system, in this case kinetic energy and an external potential, $V(x)$.

3.2 Computational Quantum Chemistry

The Hamiltonian is here taken to be (atomic units are used):

$$\begin{aligned}\hat{H} &= \hat{T}_{nuc} + \hat{V}_{N-N} + \hat{H}_{el} = \\ &= \underbrace{-\sum_A \frac{\nabla_A^2}{2M_A}}_{\hat{T}_{nuc}} + \underbrace{\sum_{A<B} \frac{Q_A Q_B}{|\mathbf{R}_A - \mathbf{R}_B|}}_{\hat{V}_{N-N}} \underbrace{-\sum_a \frac{1}{2}\nabla_a^2 + \sum_{a<b} \frac{1}{|\mathbf{r}_a - \mathbf{r}_b|} - \sum_{a,A} \frac{Q_A}{|\mathbf{R}_A - \mathbf{r}_a|}}_{\hat{H}_{el}}\end{aligned} \tag{3.4}$$

where $\hat{T}_{nuc}$ is the kinetic energy of nuclei, $\hat{V}_{N-N}$ is the Coulomb interaction between the nuclei and $\hat{H}_{el}$ is the electronic Hamiltonian, consisting of kinetic energy terms for the electrons as well as electron-electron and electron-nucleus coulomb interactions. Nuclei indices are denoted A and B while a and b are electron indices. Nuclei coordinates are given by $\mathbf{R}$ and electron coordinates by $\mathbf{r}$.

Some effects which are not correctly captured within DFT e.g. van der Waals or dispersion interactions may require corrections to the Hamiltonian, but unless stated, the employed Hamiltonian is the one in Eq. 3.4.

To solve the Schrödinger equation with the Hamiltonian in Eq. (3.4) requires several approximations due to difficulties calculating e.g. electron-electron correlations. Since nuclei masses are much larger than those of electrons, the electron motion can be considered independent of the nuclei motion, an approximation called the **Born-Oppenheimer** approximation (*37*). It follows that the motions of nuclei and electrons can be solved separately i.e.:

$$\psi_{BO}(\mathbf{r}, \mathbf{R}) = \phi(\mathbf{R})\chi(\mathbf{r}, \mathbf{R}) \tag{3.5}$$

The nuclei kinetic energy, T_{nuc} depends only on nuclei coordinates and can be treated separate from the electrons. The electronic energy E_{el} can be obtained from the electronic Hamiltonian H_{el} and the electronic wave function χ:

$$\hat{H}_{el}\chi(\mathbf{r}, \mathbf{R}) = E_{el}\chi(\mathbf{r}, \mathbf{R}) \tag{3.6}$$

The nuclear wave-function $\phi(\mathbf{R})$ is a solution to:

$$(\hat{T}_{nuc} + E_{el} + \hat{V}_{N-N})\phi(\mathbf{R}) = E_{nuc}\phi(\mathbf{R}) \tag{3.7}$$

Note that the Born-Oppenheimer approximation does not hold if nuclei movements cause transitions between electron states.

3.3 Density Functional Theory

Although mostly unknown outside of certain research fields, DFT is actually one of the most popular theoretical tools today, so much so that 12 papers on the top-100 cited papers relate to it, including two of the top 10 making it the most heavily cited concept in the physical sciences (*38*). This does not include the 1998 Nobel prize in chemistry that Walter Kohn received for its development.

Density Functional Theory, DFT is based on two **Hohenberg-Kohn** theorems (*39*) which state that:

- The ground state electron density $\rho_0(\mathbf{r})$ is uniquely determined by the external potential $v_{ext}(\mathbf{r})$.

$$v_{ext}(\mathbf{r}) \overset{1-1}{\longleftrightarrow} \rho_0(\mathbf{r}) \tag{3.8}$$

- There exists an energy functional $E_{HK}[\rho]$ (HK for Hohenberg-Kohn) with two properties:

$$E_{HK}[\rho_0] = E_0 \tag{3.9}$$

$$E_{HK}[\rho] > E_0, \text{ for } \rho \neq \rho_0 \tag{3.10}$$

where

$$E_{HK}[\rho] = \underbrace{\int v_0(\mathbf{r})\rho(\mathbf{r})d^3\mathbf{r}}_{E_{ext}[\rho]} + \underbrace{\int \psi^*[\rho]\Big(\hat{T}+\hat{U}\Big)\psi[\rho]d^3\mathbf{r}}_{F[\rho]} \tag{3.11}$$

Here, $F[\rho]$ is a universal functional containing electron kinetic energy and electron-electron interactions. The external potential v_0 contains the nuclei potentials and is system specific.

Thus, in theory it is not necessary to find the wave-function in order to calculate the total energy, instead the total electron density, $\rho(\mathbf{r})$ can be used, which is related to the wave function through

$$\rho(\mathbf{r}) = \psi^*(\mathbf{r})\psi(\mathbf{r}) = |\psi(\mathbf{r})|^2 \tag{3.12}$$

The spatial dependence of the problem is reduced from 3n spatial coordinates (3 for each electron) to only 3 spatial coordinates. Because of this DFT nominally scales as N^2. Difficulties with orbital-free DFT lies within the kinetic energy as it is difficult to express it in terms of electron density and to go beyond the Thomas-Fermi model (*40*, *41*) which takes the kinetic energy to be:

$$T_S[\rho] = C_T \int \rho^{5/3}(\mathbf{r})d\mathbf{r} \tag{3.13}$$

where C_T is a constant. Instead, most DFT codes employ a Kohn-Sham (*42*) which is based on what is called *v-representability* i.e. that there exists an effective local potential $v_{KS,0}(\mathbf{r})$ (KS = Kohn-Sham) for non-interacting particles, which corresponds to the same ground-state density $\rho_0(\mathbf{r})$ as the real external potential v_0. Since any real electronic wave-function must be anti-symmetric with respect to electron exchange, the wave-function is taken to be a Slater determinant of non-interacting one-electron spin-orbitals $\phi_i(\mathbf{r}_i)$:

$$\psi = (N!)^{-1/2}\begin{vmatrix} \phi_1(\mathbf{r}_1) & \phi_2(\mathbf{r}_1) & \cdots & \phi_n(\mathbf{r}_1) \\ \phi_1(\mathbf{r}_2) & \phi_2(\mathbf{r}_2) & \cdots & \phi_n(\mathbf{r}_2) \\ \vdots & \vdots & \ddots & \vdots \\ \phi_1(\mathbf{r}_n) & \phi_2(\mathbf{r}_n) & \cdots & \phi_n(\mathbf{r}_n) \end{vmatrix} \tag{3.14}$$

Note that the use of a single determinant fails to capture static correlation (*43*). This single determinant approach is sufficient when the ground-state is non-degenerate or when it can be constructed from a linear combination of degenerate independent electron states

which all produce the same electron density. A multi-reference approach, in which several Slater determinants describe the ground-state, becomes necessary in case of a ground-state which is generated by independent electron states with different electron densities.

It is thus possible in principle to calculate the exact energy of the ground state using a non-interaction approximation by solving the **Kohn-Sham equation** (*42*):

$$\Big(-\frac{\nabla^2}{2} + V_{ext}(\mathbf{r}) + \underbrace{\int \frac{\rho(\mathbf{r})}{|\mathbf{r}-\mathbf{r'}|} d^3\mathbf{r'}}_{v_H} + V_{xc}[\rho] \Big) \phi_i(\mathbf{r}) = \epsilon_i \phi_i(\mathbf{r}) \tag{3.15}$$

where ϕ_i are Kohn-Sham orbitals (orbitals describing the non-interacting electrons) with energy ϵ_i and where v_H is the Hartree potential describing classical electron-electron Coulomb interactions. The ground-state density is given as a sum over all occupied Kohn-Sham orbitals

$$\rho_0(\mathbf{r}) = \sum_i^N |\phi_i(\mathbf{r})|^2 \tag{3.16}$$

Rewriting Eq. (3.11) leads to an expression which can be solved iteratively:

$$E[\rho] = \int v_{KS,0}(\mathbf{r})\rho(\mathbf{r}) d^3\mathbf{r} + \frac{1}{2} \iint \frac{\rho(\mathbf{r})\rho(\mathbf{r'})}{|\mathbf{r}-\mathbf{r'}|} d^3\mathbf{r} d^3\mathbf{r'} + \sum_i^N \Big(\int \phi_i^*(-\frac{\nabla^2}{2})\phi_i d^3\mathbf{r} \Big) + E_{xc}[\rho] \tag{3.17}$$

Using the Kohn-Sham equation it is possible to calculate the (independent electron) kinetic, external, and electron-electron Coulomb energy terms exactly but not the exchange-correlation energy. For this, further elaborations are necessary.

3.3.1 Exchange-correlation functional

There are many different ways to express the exchange-correlation functional $E_{xc}[\rho]$, the simplest of which is the *Local Density Approximation* (LDA) which approximates the exchange-correlation energy at point $\boldsymbol{r}$ with that of an electron gas with density $\rho(\boldsymbol{r})$(*44*). When the functional is generalized to take spin into account, the Local Spin Density Approximation (LSDA) is arrived at:

$$E_{XC}^{LSDA}[n_\uparrow, n_\downarrow] = \int d^3\mathbf{r} n(\boldsymbol{r}) \epsilon_{XC}(n_\uparrow, n_\downarrow) \tag{3.18}$$

where $n = n_\uparrow + n_\downarrow$ is the total electron density and ϵ_{XC} is the exchange-correlation energy per particle of a uniform electron gas, an analytical expression parametrized to fit e.g. monte carlo data. An example is the LDA-PWC functional by Perdew and Wang(*45*).

LDA can be extended by including dependence on the local density gradients, arriving at the Generalized Gradient Approximation (GGA), example functionals include Perdew-Wang 1991 (PW91) (*46*) and Perdew, Burke and Ernzerhof (PBE) (*47*). GGA is expressed as:

$$E_{XC}^{GGA}[n_\uparrow, n_\downarrow] = \int d^3r f(n_\uparrow, n_\downarrow, \nabla n_\uparrow, \nabla n_\downarrow) \tag{3.19}$$

where $f(n_\uparrow, n_\downarrow, \nabla n_\uparrow, \nabla n_\downarrow)$ is a parametrized analytic function constructed as to satisfy certain physical conditions. PW91 is for instance constructed to satisfy as many exact conditions as possible, regardless of significance. This approach generally leads to an improvement over LDA, but fails in describing e.g. the linear response of the density of a uniform electron gas which LDA captures. The PBE functional on the other hand is constructed to satisfy only those conditions that are energetically significant, and thus captures the correct behavior of the uniform electron gas. Other less significant attributes which are captured by PW91 are sacrificed in this description. (*47*)

Both LDA and GGA approximations are good for e.g. metallic systems which are strongly dislocalized, but in the case of localized systems, both underestimate the band-gap in metal oxides by several electron volts (*48*). Hybrid functionals which include so called exact exchange from Hartree-Fock theory (*49*) often increase the band-gap and describe localized systems better than pure DFT functionals.The most common hybrid functionals are the PBE0 (*50*) and B3LYP (*51*) functionals.

The use of exchange-correlation functionals introduces a self-interaction error which arises from the absence of exact exchange, leading to DFT favoring delocalization (*48*). Hybrid functionals which include exact exchange may be employed to overcome this issue, but as they are computationally demanding, other methods have been developed. One of these is the LDA+U approach in which a Hubbard U potential is introduced on localized d or f states to favor localization and increase band gaps (*52–55*):

$$E_{\mathrm{LDA+U}} = E_{\mathrm{LDA}} + E_{\mathrm{Hub}} - E_{\mathrm{dc}} \tag{3.20}$$

where $E_{\mathrm{LDA+U}}$ is the DFT total energy which is being corrected, E_{Hub} is the introduced Hubbard correction to the relevant d- or f-states and E_{dc} is a term which subtracts the interaction energy of the modelled electrons from the DFT energy so as to avoid double-counting (dc). In short, the introduced U potential is designed to be repulsive for less than half-filled orbitals and attractive in the other cases, to favor localization, thereby countering effects of the self-interaction error. Issues with this method lie in its ambiguity in choosing the value of U for which many methods have been developed (*52*). Important to note is that in cases where e.g. GGA produces correct structures but fails to reproduce band gaps, a GGA+U correction may sacrifice the correct structure for an increased band gap.

3.3.2 Basis sets

The one-electron orbitals are expanded in a basis set as to be able to form the Kohn-Sham matrices, which in turn are diagonalized to find new orbitals. Possible basis sets include Slater functions (*56*), Gaussian functions (*57*), plane waves (*58*) and numerical basis set. The systems studied in this work are solid crystalline materials with translational symmetry. We thus expand the wave functions in a plane wave basis set subject to a periodic potential according to Bloch's theorem :

$$\phi_j(\mathbf{r}, \mathbf{k}) = e^{i\mathbf{kr}} u_j(\mathbf{r}) \tag{3.21}$$

and

$$u_j(\mathbf{r}) = \sum_{\mathbf{G}} C_{\mathbf{G},j} e^{i\mathbf{Gr}} \tag{3.22}$$

In principle, an infinite number of plane waves are needed to describe the system, but in practice an energy cut-off E_{cutoff} is introduced, defining the smallest length-scale of the system. Note though that the reciprocal (k-)space is discretized using a Monkhorst-Pack grid in which the Brillouin-zone is sampled on a rectangular grid of evenly spaced points with dimensions $M_x \times M_y \times M_z$ (*59*).

3.3.3 Pseudopotentials

Unlike valence electrons, core electrons do not contribute to chemical bonds. Their role is that of screening the nuclear charge, which is why they may be replaced by a pseudopotential. In such a description, only valence electrons are described explicitly i.e. only one-electron orbitals of valence electrons are considered. The pseudopotential is designed to be nodeless and equal to the real, all-electron potential outside a chosen core-radius, R_C. Often also subjected to norm-conserving conditions i.e. that the real ($\phi_{\text{all electron}}$) and pseudo ($\phi_{\text{pseudopotential}}$) wave-function both generate the same charge-density:

$$\int_0^{R_C} |\phi_{\text{all electron}}|^2 d^3\mathbf{r} = \int_0^{R_C} |\phi_{\text{pseudopotential}}|^2 d^3\mathbf{r} \tag{3.23}$$

where R_C is the core radius. For pseudopotentials to be useful, they have to be smoother than the real, all-electron potential. In the case of e.g. O-2p potentials, it can be shown that under norm-conserving conditions there is no smoother potential than the all-electron potential. By allowing violations of this condition it becomes possible to form so called ultrasoft pseudopotentials (*60*). Typically, R_C is chosen to be smaller than the radial wave-function maximum but ultrasoft potentials allows for a R_C well beyond this maximum, reducing the needed cut-off energy to describe the system. In this work, ultrasoft pseudopotentials have been employed throughout unless otherwise stated.

4 Results and Discussion

In Sec. 2, the general topic of high temperature corrosion was presented with a short introduction to oxide growth, with emphasis on alumina forming materials. In what follows, that framework is realized by means of explicit studies on different critical aspects of the corrosion process.

Oxygen ion and electron transport was emphasized within Wagner theory for the growth of a protective α-alumina scale, thus Sec. 4.1 concerns oxygen vacancy diffusion and electron transport and the effect transition metal doping has on these. The results are employed to understand early scale formation and the third element effect, where an early transient mixed oxide is formed.

In reducing environments both Al and Cr oxidation is thermodynamically stable and a thin α-alumina scale is observed to form. Micrometer-sized chromia nodules embedded in the defect-free α-Al_2O_3 scale were found susceptible to nitridation. Section 4.2 is thus concerned with understanding why nitrides are found only beneath chromia nodules and how nitrogen is transported through the chromia scale.

In reducing environments, 35 ppm H_2O acts as the single oxidant. Considering that alumina is a large band-gap insulator, electron conduction outwards to the oxide surface is inaccessible and water is instead transported as hydroxides along grain-boundaries. This transport continues until an "inner cathode" close to the alloy/scale interface is reached. Oxygen vacancies, formed at the scale/alloy interface supply electrons to the cathode, where hydroxide hydrogen becomes reduced. The fate of hydrogen during this oxidation mechanism is discussed in Sec. 4.3.1.

Enhanced oxidation was observed around surface RE-oxide particles in both oxidizing and reducing environments. Here, oxidation of Al by water is understood to be the driving force for incorporating RE-oxides functioning as "water equivalents" into alumina interfaces. This RE decoration hinders grains coarsening, leading to a thicker scale growth. In O_2 containing atmospheres, this defect rich "messy" oxy-hydroxy-hydride scale eventually becomes oxidized by O_2, upon which hydride ions are consumed and RE oxide ions precipitate. This conceptual understanding is presented in the schematic in Fig. 1.1. The incorporation of RE into alumina grain-boundaries and interfaces, and the effect it has on the eventual precipitation process is presented in Sec. 4.3.

4.1 Coupled Oxygen Vacancy and Electron Transport Mechanism

Both oxygen and electron transport has been studied adjacent to substitutionally doped transition metals, TM = Sc, Ti, Cr, V, Mn, Fe, Co, and Ni, to understand how TM dopants affect diffusion barriers and what impact they may have on early scale growth and the so-called third element effect.

4.1.1 Oxygen Vacancy Diffusion

Activation energies for oxygen vacancy diffusion have been computed as a function of vacancy charge and TM that neighbors the vacancy at the "Start"-structure, see Fig. 4.1. A decrease in activation energies is observed with increased vacancy charge and atomic number of TM dopant. Analysis of the density of states of "Start", transition state, and "End" states show that activation energies are associated with the movement of two states in the band-gap, a vacancy state and an oxygen state, see Fig. 4.2. Thus charging the vacancy reduces the occupancy of the moving vacancy state until it becomes unoccupied (doubly charged vacancy), for which the activation energy is solely decided by the movement of the oxygen state.

Moreover, the potential energy surfaces show asymmetry with respect to "Start" and "End" states in that vacancy favors TM ("Start"). This asymmetry is observed to decrease by charging the vacancies until it completely disappears in the Q=+2 case, apart for TM = Mn, Fe, Ni, for which "normal" (symmetric) states are found by varying spin state of the adatom.

Furthermore, vacancy volumes have been calculated to investigate the source of the asymmetry in the potential energy surface (APES), see Fig. 4.3. Deviations of oxygen vacancy structure, connected to its nominal charge along the reaction coordinate, that result from redox properties of the TM ions are displayed. Both "Start" and TS display little structural information and appear to have similar physical origin. The "End" state on the other hand is geometrically disconnected from TM and probes the vacancy occupation. Thus, if we follow the "End" Q=+2 line (blue), the volume associated with Ti becomes displaced with respect to the other TM. Similarly, following the "End" Q=0,+1 ,lines, Mn, Fe, and Ni are observed to become displaced. Interestingly, this is an indication of a redox process in which Ti becomes oxidized to Ti(IV) and Mn, Fe, and Ni take on an oxidation number of +II. If we now consider Start volumes again, we can observe a less clear but still significant redox of Mn, Fe, Co, and Ni at Q=0,+1 and Ti at Q=+2. Note that adatoms which undergo redox, requiring geometrical (polaronic) relaxations, also function as defect getters in the matrix, here quantified as APES. The observed APES is an effect of TM-V_O compound formation, which increases with increasing atomic number, and is affected by redox properties of the TM.

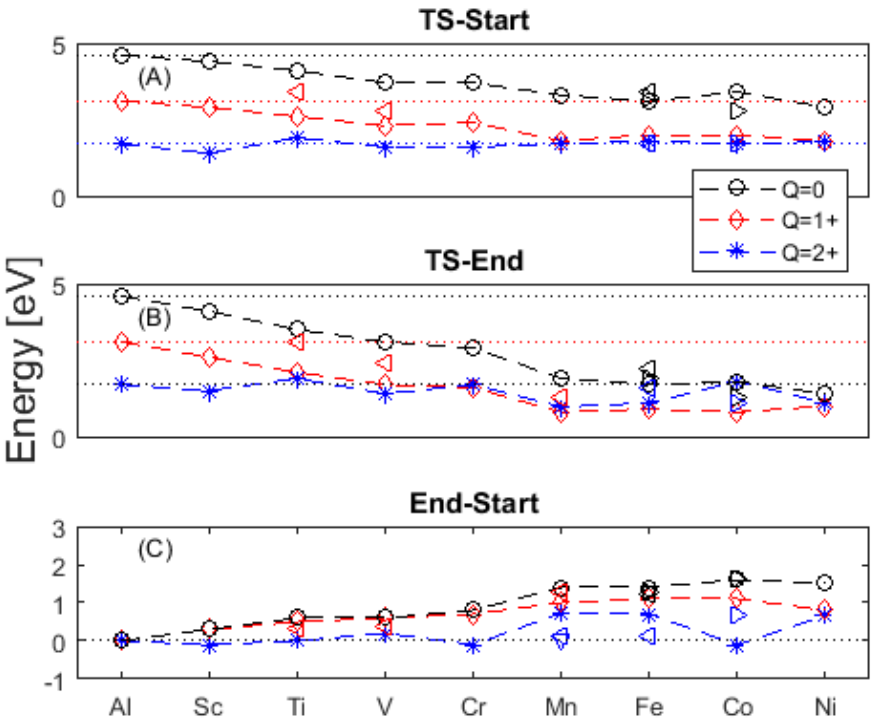

Figure 4.1: Activation energies from (A) "Start" and (B) "End" structures as well as (C) the pinning energy, "End"-"Start". Triangles denote exited spin states. Observe that Q = +2 often shows the same behavior as undoped alumina (dotted line) regardless of doping. Mn, Fe, and Ni ground states deviate from this behavior, though excited spin-states have been found which obey the earlier order. An excited Co spin-state has been found in which a pinning effect is observed for Q = +2.

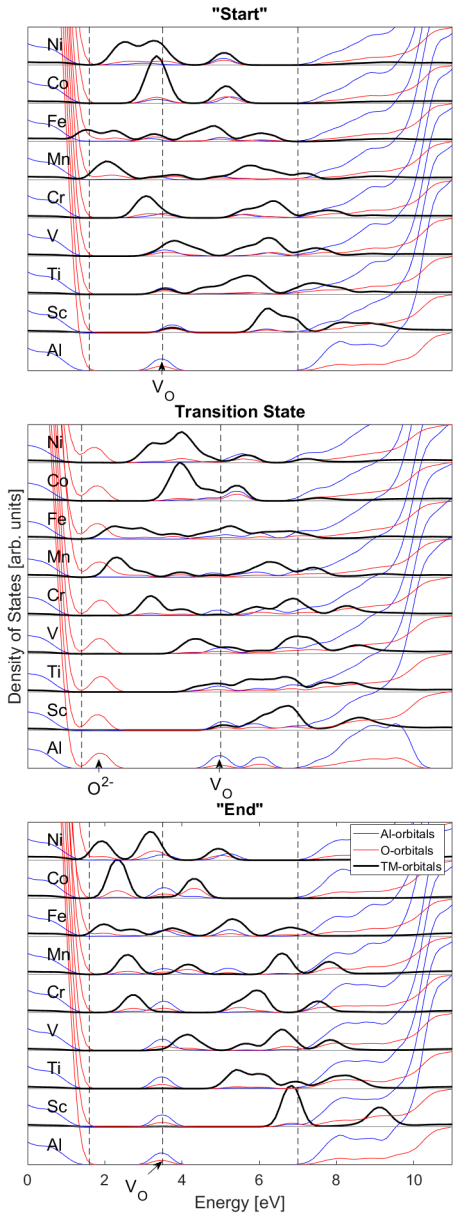

Figure 4.2: Total density of states (DOS) subdivided into transition metal TM, Al, and O partial density of states (PDOS). "Start", transition state, "End": TM bands are split and down-shifted with increasing atom number. "Start"; the oxygen vacancy V_O band overlaps with the TM states. Transition state; the TM-V_O overlap remains, and in addition an O^{2-} state comes out of the valence band. "End"; TM-V_O overlap disappears as seen in mismatch of TM and V_O band energies. Dotted lines emphasize positions of top of valence band and bottom of conduction band.

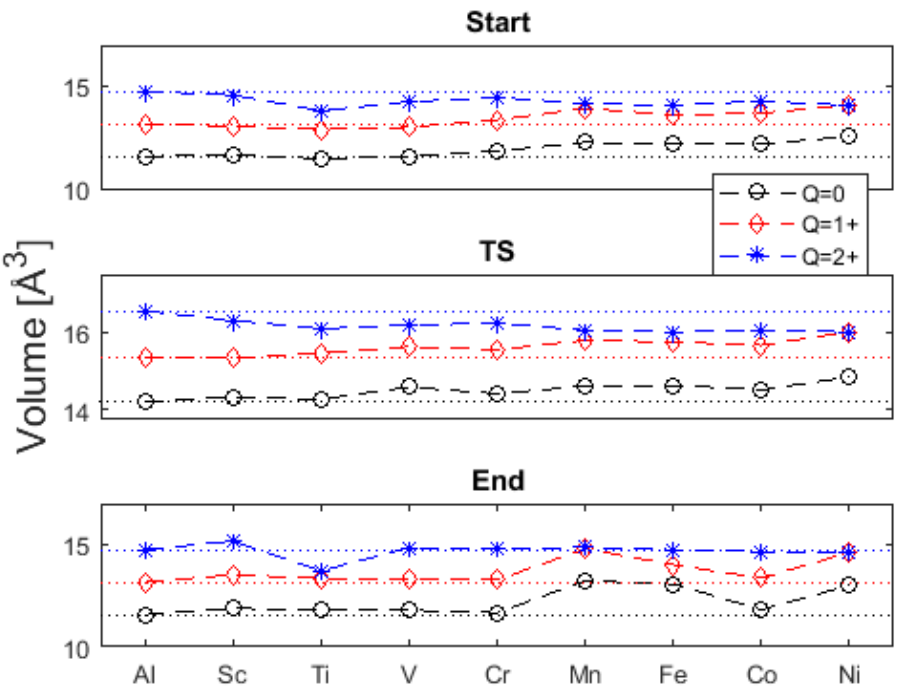

Figure 4.3: Computed vacancy volumes for "Start", TS, and "End". "Start" and TS show similar behavior where Q = 0, +1 have an increase in volume for Mn, Fe, Co, and Ni while Q = +2 seems to decrease with atomic number. "End" state, being physically removed from the TM tests the vacancy charge. Ti(Q = +2) shows the Ti to donate an electron to the vacancy, which takes on a +1 charge state. Mn, Fe, and Ni are reduced in Q = 0, +1.

4.1.2 Electron Transport

Here, electron transfer between two distant oxygen vacancies is discussed. The vacancies are in the proximity of either Al (pure alumina) or TM = Sc, Ti, V, Cr, Mn, Fe, Co, Ni. Activation energies, reaction energies and corresponding volume changes have been computed for the following five reactions:

$$B(P_y^0; P_x^{+1}) \rightarrow B(P_y^{+1}; P_x^0) \tag{4.1}$$

$$B(P_y^0; P_x^{+2}) \rightarrow B(P_y^{+1}; P_x^{+1}) \tag{4.2}$$

$$B(P_y^{+1}; P_x^{+1}) \rightarrow B(P_y^{+2}; P_x^0) \tag{4.3}$$

$$B(P_y^{+1}; P_x^{+2}) \rightarrow B(P_y^{+2}; P_x^{+1}) \tag{4.4}$$

$$B(P_y^0; P_x^{+21}) \rightarrow B(P_y^{+2}; P_x^0) \tag{4.5}$$

where $B(P_y^{Q1}, P_x^{Q2})$ is the notation for two spatially separated polarons, a bipolaron, with nominal charges Q1 and Q2, and adjacent to x,y = Al, Sc,..., Ni. Additionally, the position of the crossing, X_{AB} between $\Psi_A(q)$ and $\Psi_B(q)$ along reaction coordinate q, was computed. It's important to note that the calculated activation energy is the energy required to allow tunneling and not the potential barrier which is tunneled through.

All possible pairwise electron transfers have been captured and are reported in the supplementary information to Paper I, but the focus here lies on two specific subsets. First, those between equivalent oxygen vacancy compositions, i.e. where $x = y = Al, Sc, ..., Ni$, which corresponds to a high density doping regime (when $x = y \neq Al$), see Fig. 4.4. Secondly, in between TM-V_O associated electron transfers, any number of Al-Vo associated transfers may occur, starting with the electron transfer from a TM-V_O site to an Al-V_O site and ending with the inverse electron transfer reaction, thus this corresponds to $x = Al, Sc, ..., Ni$, $y = Al$, see Fig. 4.5 for activation and reaction energies, and corresponding volume changes.

The activation energies for electron transfer is calculated to be around 0.5 eV, significantly lower than activation energies for oxygen vacancy diffusion (2 eV for $V_O^{\bullet\bullet}$), suggesting this to be a viable electron transport path.

In Fig. 4.5 similarly to vacancy trapping adjacent to TM, electrons are trapped in vacancies adjacent to TM in that ΔE_B^* increases with atomic number. Note also that the processes involving the reduction P_E^{+1} to P_E^0 are relatively constant up until E=Mn, where the energy converges, this due to redox effects coming into play for Q=0,+1.

4.1.3 Third Element Effect

The effect of adding Cr to a binary Fe-Al alloy was discussed in Ch. 2 with emphasis on decreasing Fe and internal Al oxidation as well as promoting α-Al_2O_3 formation. The question becomes whether the choice of Cr as third element in a Fe-TM-Al ternary alloy is unique. The criteria in literature for a good third element states the third element oxide stability to be between the oxides of the base metal and the scale forming element. In the studied set of TMs; Sc, Ti, V, Cr, and Mn fulfill this condition. Although miscibility of third element in alumina is emphasized, this was not studied here directly. It is possible, however, to argue that the stability of the TM(III) state may be employed as

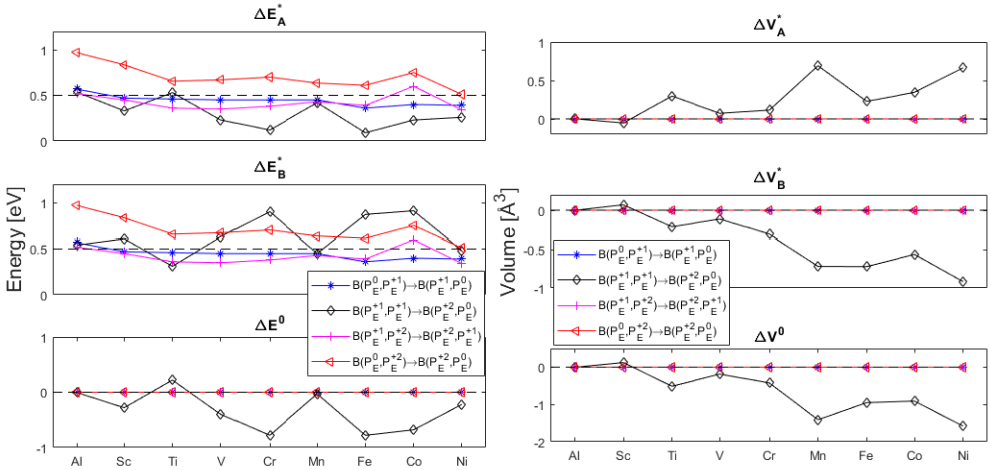

Figure 4.4: (left) Activation and reaction energies ΔE_A^*, ΔE_B^*, and ΔE^0 and (right) corresponding volume changes for the symmetric electron transfer process, $x = y = E$.

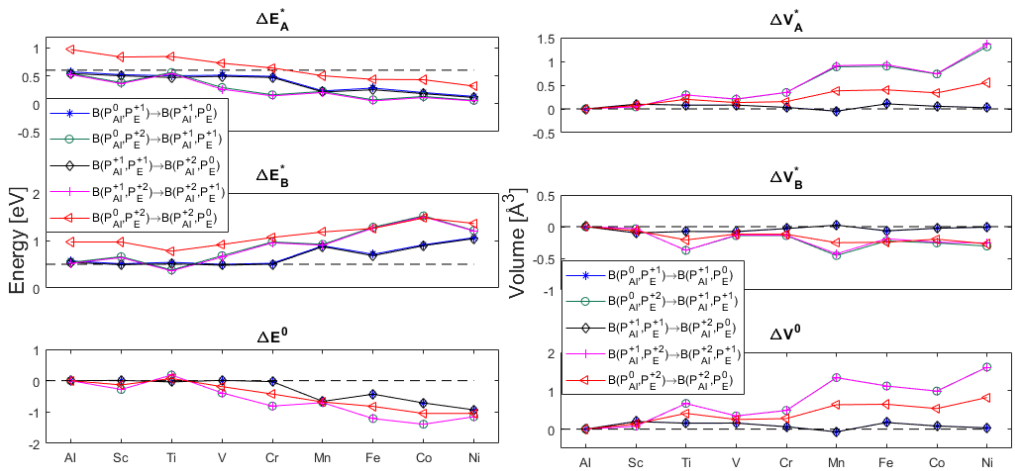

Figure 4.5: (left) Activation and reaction energies ΔE_A^*, ΔE_B^* and ΔE^0 and (right) corresponding volume changes for the asymmetric electron transfer from an Al surrounding ($y = Al$) to a TM associated surrounding.

an indicator, thus Ti and Mn both exclude themselves by maintaining oxidation states differing from the +III state of Al. As Sc, although maintaining a +III oxidation state, shows similar oxygen vacancy and electron transport barriers as Al, it is not clear how it may facilitate the transformation of the initial metastable oxide. Thus, we arrive at two possible candidates for third elements in a Fe-TM-Al alloy: V and Cr. Both show similar oxygen and electron barriers, and other properties than those discussed here must be used discriminate between two.

4.2 Internal Nitridation in Alumina Formers

In reducing, 95% N_2/5% H_2 environments at 900°C, FeCrAl(RE) alloys show AlN and CrN/Cr_2N formation beneath chromia nodules scattered across the surface. The chromia patches are oxidized chromium carbide particles which are formed during alloy manufacture. Paper II discusses necessary conditions for N_2 dissociation on alumina and chromia surfaces where two surface conditions were studied, 0%, and 50% oxygen coverage. Paper III contains a short study on the nitrogen adsorption on 0%, and 50% oxygen covered yttria surfaces.

Furthermore, nitrogen transport through chromia scales was studied as to show that (ionic) nitrogen transport channels exist through the chromia scale.

4.2.1 Nitrogen Adsorption

The employed alumina and chromia slab models contain two coordinately unsaturated metal sites (CUS) denoted [-,-]. Thus [-,O], or [O,-] implies that one of the two sites is occupied by oxygen. The calculations performed here are of the general reaction:

$$MN(s) + [-;A]M_{2x}O_{3x}(slab) \rightarrow M(s) + [N;A]M_{2x}O_{3x}(slab) \tag{4.6}$$

where M=Al, Cr and A=-, N, or O, denoting whether the CUS site is vacant or occupied by nitrogen or oxygen. The experimental enthalpy of formation of $MN(s)$ is used to shift the calculated enthalpy to arrive at the more relevant surface nitridation enthalpy, denoted with a tilde:

$$\Delta\widetilde{H}_M^{N;-} = \Delta H_M^{N;-} - \Delta H_{exp}[MN(s)] \tag{4.7}$$

The reaction in this case becomes:

$$\frac{1}{2}N_2 + [-;A]M_{2x}O_{3x}(slab) \rightarrow [N;A]M_{2x}O_{3x}(slab) \tag{4.8}$$

And analogously for the case:

$$2MN(s) + [-;-]M_{2x}O_{3x}(slab) \rightarrow 2M(s) + [N;N]M_{2x}O_{3x}(slab) \tag{4.9}$$

Note that the entropy contribution for N_2 at 900°C, 180 kJ/mol has been taken into consideration.

Employing the earlier notations, N_2 adsorption energies on bare alumina and chromia surfaces, i.e.:

$$\frac{1}{2}N_2 + [-;-]M_{2x}O_{3x}(slab) \rightarrow [N;-]M_{2x}O_{3x}(slab) \tag{4.10}$$

are found to be $\Delta\widetilde{H}_{Al}^{N;-}$ = 180 kJ/(mol N_2) and $\Delta\widetilde{H}_{Cr}^{N;-}$ = -40 kJ/(mol N_2). To test the sensitivity of surface coverage of oxygen, calculations with 50% coverage are considered, see the following reaction:

$$\frac{1}{2}N_2 + [-;O]M_{2x}O_{3x}(slab) \rightarrow [N;O]M_{2x}O_{3x}(slab) \tag{4.11}$$

Here, $\Delta\widetilde{H}_{Al}^{N;O}$ = +39.1 kJ/mol and $\Delta\widetilde{H}_{Cr}^{N;O}$ = -135 kJ/mol. Instead of nitrogen and oxygen occupying one CUS site each, on alumina there is NO formation, implying an inability to co-chemisorb N and O to the alumina surface.

Finally, to see the effect of full N coverage, the same calculations were performed with all sites occupied by N:

$$N_2 + [-;-]M_{2x}O_{3x}(slab) \rightarrow [N;N]M_{2x}O_{3x}(slab) \tag{4.12}$$

Results show $\Delta\widetilde{H}_{Al}^{N;N}$ = -93.9 kJ/mol and $\Delta\widetilde{H}_{Cr}^{N;N}$ = -135 kJ/mol. In this case residual N-N bonding adds to the stability on alumina. On chromia however, there is complete dissociation.

Similar calculations on yttria surfaces showed yttria to be able to adsorb and dissociate N_2 on bare, 0% O-covered surfaces while N-adsorbtion could not be stabilized on a 50% O-covered surface. There is a fundamental differences between alumina, yttria, and chromia scales and the availability of CUS sites, crucial for the nitrogen adsorption and dissociation. Chromia, unlike alumina and yttria is known for having several oxidation states e.g. Cr(III) and Cr(IV), allowing for Cr oxidation in order to reduce N_2, which requires 6 electrons. Additionally, there are two driving forces for maintaining a high CUS coverage on chromia surfaces:

Firstly, the superior stability of alumina ($\Delta H_f(Al_2O_3)$=-1675 kJ/mol) compared to chromia ($\Delta H_f(Cr_2O_3)$=-1134 kJ/mol) implies that as long as aluminum is in the vicinity of chromia it will reduce the chromia nodules. This channel is closed for yttria as its stability is higher than that of alumina ($\Delta H_f(Y_2O_3)$=-1905 kJ/mol), and there is no driving force to maintain CUS coverage on this surface. Secondly, the drive for internal nitridation of aluminum whereby AlN is formed (ΔH_f(AlN)=-318 kJ/mol, compare with ΔH_f(CrN)=-117 kJ/mol), will work to incorporate nitrogen into chromia.

4.2.2 Nitrogen Absorption in Chromia Scales

Chromia scales were shown to be more likely than alumina to chemisorb and dissociate N_2. In order for internal nitridation to occur in the alloy beneath the chromia scale, nitrogen ions need to be transported through the chromia lattice. This transport is here investigated in the form of transient chromium oxy-nitrides, which are formed by substitutional nitrogen-doping in chromia. To maintain charge balance one oxygen atom is removed for every two nitrogen in the unit cell.

As long as unreacted Al is in the vicinity of the chromia path, there will be no build up of any barrier chromia scale. The chromium oxy-nitride formation reaction, required for nitrogen diffusion is represented by the following reaction:

$$Cr_2O_3(s) + \frac{y}{2}N_2(g) + yAl(s) \rightarrow Cr_2N_yO_{3-\frac{3y}{2}}(V_O^{**})_{\frac{y}{2}}(s) + \frac{y}{2}Al_2O_3(s) \tag{4.13}$$

Chromia can be thought of as to be in contact with two media, N_2(g) and Al(s) in the alloy since Fe can not reduce chromia. Nitrogen reacts with chromia to form oxy-nitrides and the left-over oxygen subsequently reacts with Al to form alumina:

$$N_2(g) + 2Al(s) + Cr_{12}O_{18}(s) \rightarrow Cr_{12}N_2O_{15}(V_O^{**})(s) + Al_2O_3(s) \tag{4.14}$$

For which a reaction enthalpy of ΔH_r = -514 kJ/mol is arrived.

A plateau is in sight as the following, Al_2O_3 driven reaction:

$$N_2(g) + 2Al(s) + Cr_{12}N_2O_{15}(V_O^{**})(s) \rightarrow Cr_{12}N_4O_{12}(V_O^{**})_2(s) + Al_2O_3(s) \tag{4.15}$$

has a reaction enthalpy of ΔH_r = -570 kJ/mol. The limiting case, CrN formation is exothermic by ΔH_r = -750 kJ/mol:

$$N_2(g) + Cr_2O_3(s) + 2Al(s) \rightarrow 2CrN(s) + Al_2O_3(s) \tag{4.16}$$

A reason why the transient chromium oxy-nitride has not yet been found experimentally might be that it disproportions into CrN and Cr_2O_3:

$$Cr_{12}N_2O_{15}(V_O^{**})(s) \rightarrow 5Cr_2O_3(s) + 2CrN(s) \tag{4.17}$$

which is exothermic, $\Delta H_r = \sim$-200 kJ/mol. The results are summarized in the energy landscape in Fig. 4.6.

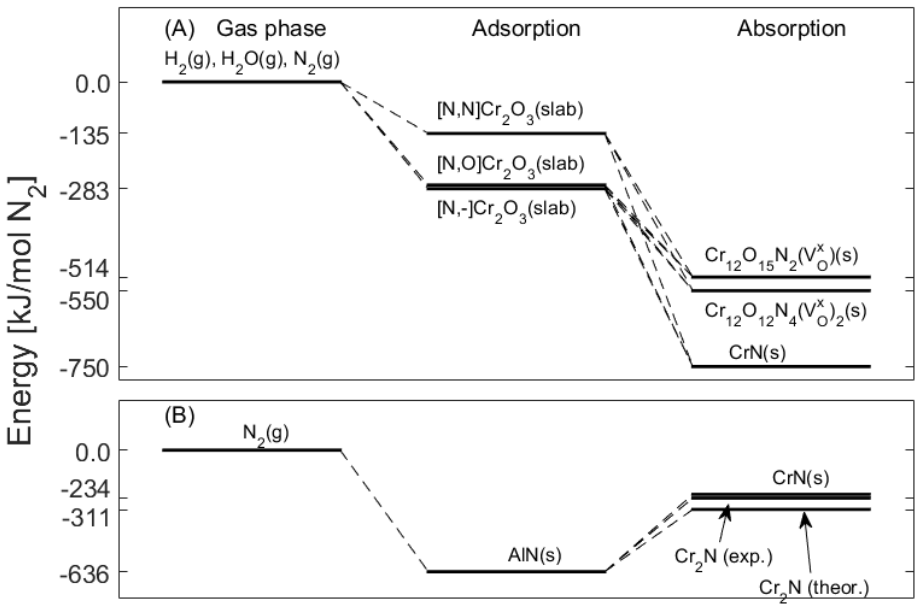

Figure 4.6: (A) Energy landscape for N_2 incorporation into the alloy to by forming transient chormium oxy-nitrides. (B) Net nitridation enthalpies of aluminium and chromium.

4.3 Early H_2O/RE Oxidation Mechanism

Here, a water mediated RE decoration of alumina grain-boundaries is discussed. This is the topic of Papers III-V, in which first the fate of hydrogen during Al-oxidation by water is discussed (Paper III). Paper IV regards the water-mediated Y-decoration of alumina grain-boundaries and its impact on early oxidation. Lastly, Paper V extends the results from Paper IV to several REs: Al(III), Sc(III), Y(III), La(III), Ce(III) as well as Ti(IV), Zr(IV), Hf(IV) and Ce(IV), focusing on the effect of ionic radius and charge.

4.3.1 Fate of Hydrogen

In reducing environments (95% N_2, 5% H_2, 35 ppm H_2O) a thin adhesive α-alumina scale is formed despite the low water content which acts as the main oxidant. With water as an oxidant, it is crucial to first understand how the cathode product, hydrogen is disposed of. The oxidation process by water is thus envisioned to occur in three steps:

1. Oxygen vacancies are formed at the oxide/alloy interface and diffuse to the surface.
2. Hydroxide oxygen diffuses into the vacancy, leaving a hydride to accommodate the surface oxygen vacancy.
3. Re-hydroxylation of the vacant surface state by H_2O whereby, (A) H_2 evolves through H^--H^+ recombination, or (B) the surface hydride enters an oxygen vacancy.

As a starting point, we note that oxidation of aluminum by surface hydroxide oxygen is exothermic as expected:

$$\begin{gathered}\frac{2}{3}Al(s) + (OH)_{12}@Al_2O_3(slab) \rightarrow \frac{1}{3}Al_2O_3(s) + (OH)_{11}H@Al_2O_3(slab) \\ \Delta\mathrm{E} = -1.60 \text{ eV}\end{gathered} \tag{4.18}$$

A following hydrogen evolution by recombining the resulting H^- with a vicinal proton is on the other hand endothermic:

$$\begin{gathered}(OH)_{11}H@Al_2O_3(slab) \rightarrow H_2(g) + (OH)_{10}O@Al_2O_3(slab) \\ \Delta\mathrm{E} = 0.96 \text{ eV}\end{gathered} \tag{4.19}$$

Note though that if the entropic contribution at 1200 K ($\sim 900°$C) is taken to be the standard molar entropy of H_2(g) which is $\sim 130\frac{\mathrm{J}}{\mathrm{mol\ K}}$, a resulting reaction energy of ~ -0.6 eV is arrived at. We can also consider a possibility of depositing hydrogen into neutral oxygen vacancies in the oxide lattice as hydrides:

$$\begin{gathered}H_2O(g) + (OH)_{11}H@Al_2O_3(V_O)_2(slab) \rightarrow (OH)_{12}@Al_2O_3(H@V_O)_2(slab) \\ \Delta\mathrm{E} = -0.26 \text{ eV}\end{gathered} \tag{4.20}$$

At a first glance this channel for hydrogen disposal might seem superior to hydrogen evolution, but we have to consider two facts; first, loss of entropy of H_2O is not taken into consideration, and secondly, GGA underestimates the band-gap, why these results

must be met with caution. If we instead consider the hydroxylated alumina interface, the band gap is 1.5 times larger than in the free standing slab, making the extrinsic states inaccessible unlike the slab model. The same reaction in the alumina interface becomes:

$$H_2O(g) + (OH)_{11}H@Al_2O_3(V_O)_2(GB) \rightarrow (OH)_{12}@Al_2O_3(H@V_O)_2(GB) \\ \Delta\text{E} = 1.47 \text{ eV} \tag{4.21}$$

Thus forbidding the deposition of protons into vacancies in the oxide lattice. With regards to hydrogen deposition, we expect hydrogen not to be found in the alumina lattice but instead at alumina interfaces or grain-boundaries in the form of hydroxide or hydrides. A possible channel for disposing hydrogen may be hydrogen pick-up in the alloy at the oxide-alloy interface.

4.3.2 Interplay of Water and RE on FeCrAl(RE) Oxidation

We first note that the spontaneous incorporation of yttria into alumina grain-boundaries i.e.

$$\alpha\text{-}\mathrm{Al_2O_3}+\mathrm{Y_2O_3} \rightarrow \mathrm{GB}(\mathrm{OY_{2/3}O})\mathrm{GB} \\ \Delta\mathrm{H} = +1.34 \text{ eV/Y} \tag{4.22}$$

is endothermic. But coupled with Al-oxidation by water, upon which the RE-oxide acts as a water equivalent, the RE decoration reaction becomes exothermic. This is modelled as the the replacement of 3(4) H^+ for a RE(III/IV) in the hydroxylated alumina interface:

$$\text{RE(III): } \frac{x}{2}RE_2O_3 + xAl + (\text{"}H_2O\text{"})_{12}@GB \rightarrow \\ \frac{x}{2}Al_2O_3 + [RE_2O_3]_{x/2}(\text{"}H_2O\text{"})_{12-\frac{3x}{2}}@GB + \frac{3x}{2}H_2 \tag{4.23}$$

where RE(III)=Sc, Y, La, Ce, and $x = 1, 2, ..., 8$. For RE(IV) we arrive at a similar equation:

$$\text{RE(IV): } xREO_2 + \frac{4x}{3}Al + (\text{"}H_2O\text{"})_{12}@GB \rightarrow \\ \frac{2x}{3}Al_2O_3 + [REO_2]_x(\text{"}H_2O\text{"})_{12-2x}@GB + 2xH_2 \tag{4.24}$$

where RE(IV)=Ti, Zr, Hf, Ce, and $x = 1, 2, ..., 6$ and where an Al vacancy is introduced for each triad of RE(IV). The reaction energies and temperatures are shown in Fig. 4.7.

Thus by coupling the RE decoration reaction with Al-oxidation by water, it becomes exothermic for all RE at temperatures above 900° C apart from Y which becomes exothermic first at 37.5% coverage. This implies that the Y-decoration occurs such that a supersaturation beyond 37.5% precedes the expansion of the Y-decoration front.

The separation of RE(III) and RE(IV) originates from the fact that $\frac{3}{2}\mathrm{H_2}$ evolves from $\frac{3}{2}\mathrm{H_2O}$ and 2 $\mathrm{H_2}$ from 2 $\mathrm{H_2O}$ respectively. Furthermore, a larger spread in energies among the RE(III) as opposed to RE(IV) is observed. This spread is found to correlate to a

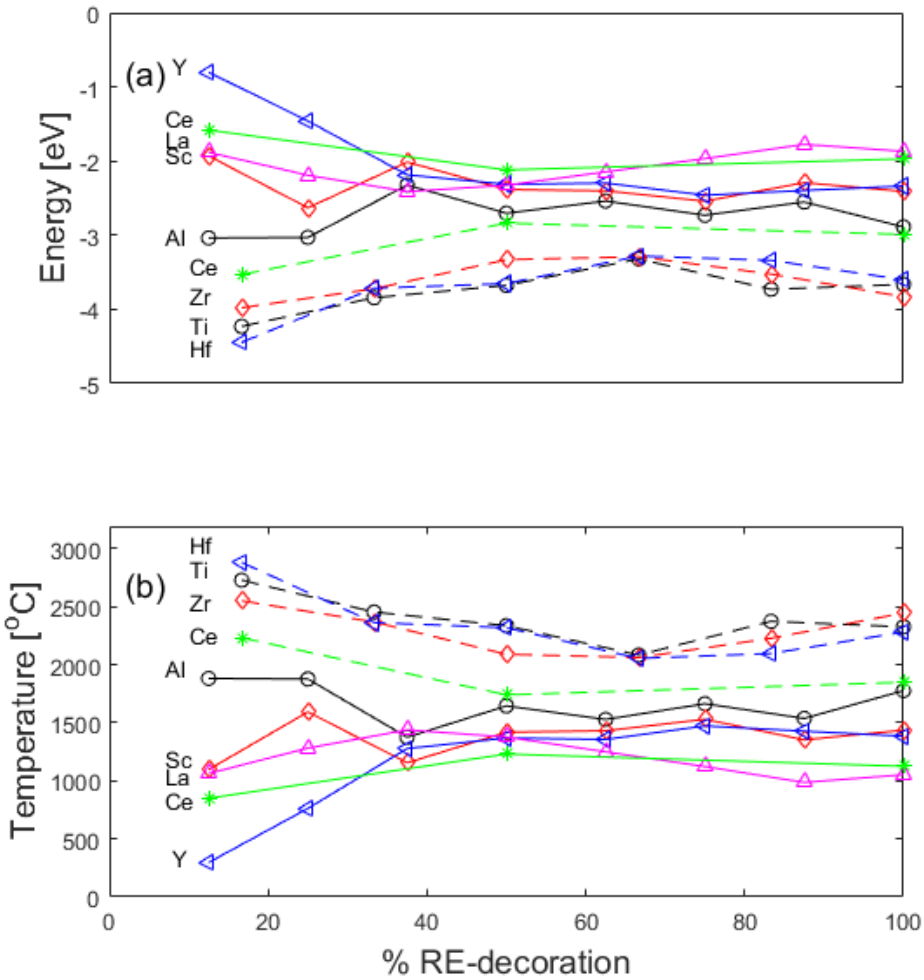

Figure 4.7: (a) Reaction energies and (b) temperatures for the RE/H_2O co-decoration reaction. The temperature is proportional to the inverse energy. The +III and +IV cations are separated in bundles with the +III cations showing larger variations, especially at lower coverages. Ce(IV) is vertically displaced with respect to the other RE(IV), this is due to its larger ionic radius as seen in Fig. 4.9

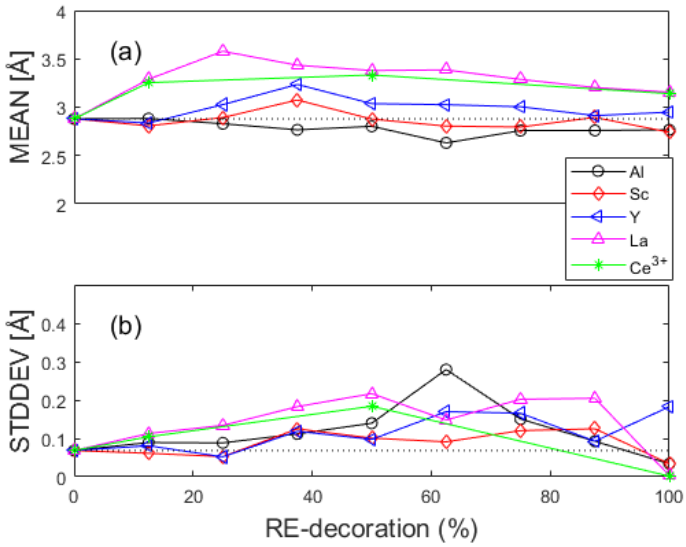

Figure 4.8: (a) Mean and (b) corresponding standard deviations of the oxygen-oxygen distances between the two interface planes for RE(III). It is clear that larger RE increase the interface size due to confinement effects.

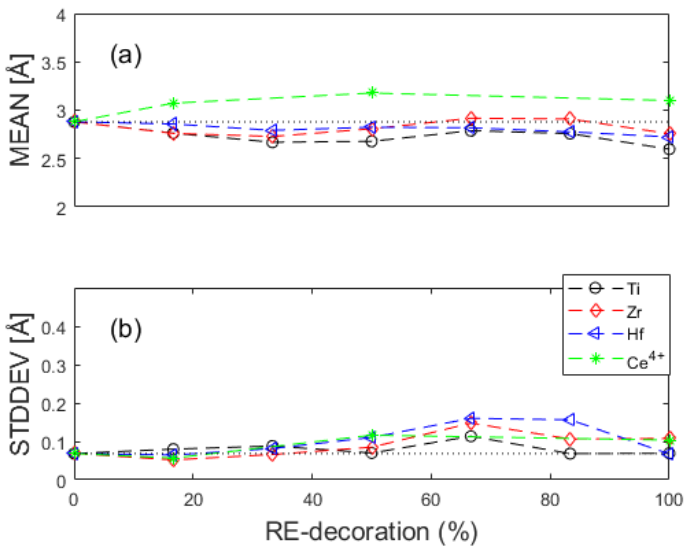

Figure 4.9: (a) Mean and (b) corresponding standard deviations of the oxygen-oxygen distances between two RE(IV) decorated interface planes. Apart from Ce(IV), there is no observed interface distance increase with RE ion size.

larger variation in grain-boundary width, as quantified by O-O distances across interfaces between alumina slabs, see Fig. 4.8 and 4.9. With the exception of Ce(IV), no variation is found for the RE(IV), regardless of size. At a first sight, this might appear counter-intuitive, but may partly be understood to originate from charge neutrality conditions, enforcing every three RE(IV) in the interface to coexist with a cationic vacancy. Thus, as cation radius increases from $R(Ti^{4+})<R(Zr^{4+})\sim R(Hf^{4+})<R(Ce^{4+})$, lateral deformations may be understood to relax the corresponding build-up of stress in the case of the former three. Ce(IV) which has an ionic radius compared to that of Y(III), is exempted from this and comes out intermediate to the two classes. The inability of RE(III) to relax stresses laterally is reflected by the larger grain-boundary widths, this is especially clear when comparing Y(III) with La(III). While smaller RE(III) e.g. Al and Sc may be accommodated, the grain-boundary decoration by larger RE(III) forces a separation between the interface planes and causes stresses.

Inasmuch as an enhanced early oxidation is understood to facilitate the transformation into a more adherent alumina scale, build up of stresses, as observed for RE(III) and Ce(IV) may support a more rapid RE oxide precipitation process. RE(IV) are then understood to support enhanced oxidation by keeping grain-boundaries open as "water" transport channels longer than RE(III) and Ce(IV).

5 Summary and Future Work

The applicability of the phenomenological Wagner theory for alumina scale growth was explained. Being a large band gap insulator, electron transfer through the oxide scale is problematic. Here, Marcus theory was employed in a bipolaron setting to quantify necessary conditions for electron hopping conductivity, where oxygen vacancies provide the required impurity states in the band gap.

The third element effect was given a local meaning at early stages of scale growth in a systematic study comparing Sc, Ti, V, Cr, Mn, Fe, Co, and Ni employed as guest ions in an alumina lattice. Ranking the affinity to oxygen vacancies V_O, a generic defect in the oxide, only Cr and V displayed ideal intermediate affinities, i.e. intermediate to Fe and Al. Thus, upon initial exposure to air, rapid formation of non-specific oxide is formed. Subsequently, this transient oxide undergoes transformations whereby V_O defects are transferred into the iron oxide, rendering it reduced, while chromia is formed. At a third stage, chromia acts oxidant towards aluminum to render the resulting protective alumina defect free.

FeCrAl(Y) is employed as roller material for transporting steel through the heat treatment furnace during manufacturing. In nominally reducing conditions, e.g. 5% H_2 95% N_2 to avoid oxidation on steel products, impurity water is sufficient to form a protective oxide scale on these rollers. A mechanism for permeation of nitrogen through micrometer-sized transient chromia nodules embedded in defect free alumina scales acting "windows" was demonstrated. It is the oxidation of aluminum by chromia that allows transient chromium oxy-nitrides to form, thus paving the way for nitrogen to be absorbed by the alloy where it forms stable internal aluminum nitrides, thus consuming the source of Al crucial for sustaining the protective alumina scale.

A long-standing issue concerns the crucial impact of water during alloy oxidation. This topic has been addressed by us focusing on how water permeates the oxide scale by hydrolysis thus achieving hydroxylated interfaces between oxide grains. The interplay of RE and water vapor during alumina scale formation on FeCrAl(Y) was recently unraveled and generalized by us to apply to a wider class of RE, i.e. Y, La, Zr, Hf, Ce. It was shown to assist water to jointly produce a nano-granular RE decorated rapidly growing "messy" transient aluminum oxy-hydroxy-hydride scale. At a second stage, this messy oxide is oxidized by O_2, the hydride ions become consumed whereby the RE ions spontaneously form microscopic precipitates. Inasmuch as the Al content is $\gtrsim$ 5 at.% in the FeCrAl(RE), the rapid initial oxide growth offers a means to harvest alumina so that a sufficiently thick and well adherent alumina scale is formed.

A future outlook should include generalizing the modelling of oxide scaling and corrosion initiated, to address

(i) "hot corrosion" in waste fueled boilers

(ii) salt melt induced corrosion in solar energy powered turbine applications

(iii) the impacts of hydrogen,

   a. in solid oxide fuel cell applications, being picked-up and permeated through stainless steel interconnects

b. in nuclear energy applications, permeating chromium coatings to be picked up by zircaloy cladding materials

Such and similar targets provide vehicles for further explorations of the fruitful interface between solid state chemistry and solid state physics utilizing the non-equilibrium phenomenology of high temperature corrosion for the benefit of both fields

References

(*1*) G. H. Koch et al. "Cost of corrosion in the United States". *Handbook of Environmental Degradation of Materials*. William Andrew Publishing, 2005.

(*2*) B. Hou et al. The cost of corrosion in China. *npj Materials Degradation* **1** (2017).

(*3*) H. Asteman et al. Influence of Water Vapor and Flow Rate on the High-Temperature Oxidation of 304L; Effect of Chromium Oxide Hydroxide Evaporation. *Oxidation of Metals* **54** (2000), 11–26.

(*4*) B. Jönsson and A. Westerlund. Oxidation Comparison of Alumina-Forming and Chromia-Forming Commercial Alloys at 1100 and 1200 °C. *Oxidation of Metals* **88** (2017), 315–326.

(*5*) K. Terrani, S. Zinkle, and L. Snead. Advanced oxidation-resistant iron-based alloys for LWR fuel cladding. *Journal of Nuclear Materials* **448** (2014), 420–435.

(*6*) K. Field et al. *Handbook on the Material Properties of FeCrAl Alloys for Nuclear Power Production Applications*. Tech. rep. Oak Ridge National Laboratory, 2017.

(*7*) J. Stringer. The reactive element effect in high-temperature corrosion. *Materials Science and Engineering: A* **120-121** (1989), 129.

(*8*) P. Hou. Impurity Effects on Alumina Scale Growth. *Journal of the American Ceramic Society* **86**.4 (2003), 660–668.

(*9*) B. A. Pint and K. B. Alexander. Grain Boundary Segregation of Cation Dopants in a-Al2O3 Scales. *Journal of The Electrochemical Society* **145** (1998), 1819.

(*10*) D. Young. *High Temperature Oxidation and Corrosion of Metals*. Elsevier, 2008, p. 25.

(*11*) Z. Zhang et al. Criteria for the formation of protective Al2O3 scales on Fe–Al and Fe–Cr–Al alloys. *Corrosion Science* **48** (2006), 741–765.

(*12*) J. P. Wilber, M. Bennett, and J. Nicholls. Life-time extension of alumina forming FeCrAl–RE alloys: influence of alloy thickness. *Materials at High Temperatures* **17** (2000), 125–132.

(*13*) P. Kofstad et al. International workshop on "New Fundamentals of Scale Growth". *Oxidation of Metals* **32** (1989), 125–166.

(*14*) A. Heuer and K. Lagerlöf. Oxygen self-diffusion in corundum (alpha-Al2O3): A conundrum. *Philosophical Magazine Letters* **79** (1999), 619–627.

(*15*) P. Kofstad. *High Temperature Corrosion*. Elsevier Applied Science Publishers LTD, 1988.

(*16*) A. H. Heuer et al. Alumina Scale Formation: A New Perspective. *Journal of the American Ceramic Society* **94**.S1 (2011), 146–153.

(*17*) C. Badini and F. Laurella. Oxidation of FeCrAl alloy: Influence of temperature and atmosphere on scale growth rate and mechanism. *Surface and Coatings Technology* **135** (2001), 291–298.

(*18*) A. Atkinson. Wagner Theory and Short Circuit Diffusion. *Materials Science and Technology* **4**.December (1988), 1046–1051.

(*19*) A. Heuer et al. On the growth of Al2O3 scales. *Acta Materialia* **61** (2013), 6670–6683.

(*20*) P. Sarrazin et al. *Mechanisms of High Temperature Corrosion: A Kinetic Approach*. Trans Tech Publications Ltd., 2008.
(*21*) D. Naumenko, B. Pint, and W. Quadakkers. Current Thoughts on Reactive Element Effects in Alumina-Forming Systems: In Memory of John Stringer. *Oxidation of Metals* **86**.1-2 (2016), 1.
(*22*) K. Unocic et al. STEM and APT characterization of scale formation on a La,Hf,Ti-doped NiCrAl model alloy. *Micron* **109** (2018), 41.
(*23*) F. Morin, G. Beranger, and P. Lacombe. Limits of Application for Wagner's Oxidation Theory. *Oxidation of Metals* **4** (1972), 41.
(*24*) C. Wagner. Beitrag Zur Theorie des Anlaufvorgangs. *Zeitschrift für Physikalische Chemie* **21B** (1933), 25.
(*25*) W. J. Quadakkers et al. Growth Rates of Alumina Scales on Fe–Cr–Al Alloys. *Oxidation of Metals* **61** (2004), 17–37.
(*26*) N. Cabrera and N. F. Mott. Theory of the oxidation of metals. *Reports on Progress in Physics* **12** (1949), 163–184.
(*27*) F. Fehlner and N. Mott. "Oxidation in the Thin-Film Range". *Oxidation of Metals and Alloys*. Ed. by D. Douglass. American Society for Metals, 1970. Chap. 3, pp. 37–62.
(*28*) C. Geers and I. Panas. Impact of Grain Boundary Density on Oxide Scaling Revisited. *Oxidation of Metals* **55** (2019), 91.
(*29*) H. E. Evans, A. T. Donaldson, and T. C. Gilmour. Mechanisms of Breakaway Oxidation and Application to a Chromia-Forming Steel. *Oxidation of Metals* **52** (1999), 379–402.
(*30*) N. Birks, G. Meier, and F. Pettit. *Introduction to the high temperature oxidation of metals*. Cambridge University Press, 2006.
(*31*) N. Govind et al. A generalized synchronous transit method for transition state location. *Computational Materials Science* **28** (2003), 250–258.
(*32*) A. Heuer. Oxygen and aluminum diffusion in alpha-Al2O3: How much do we really understand? *Journal of the European Ceramic Society* **28** (2008), 1495.
(*33*) J. Harding, K. Atkinson, and R. Grimes. Experiment and Theory of Diffusion in Alumina. *Journal of the American Ceramic Society* **86** (2003), 554.
(*34*) U. Aschauer, P. Bowen, and S.C.Parker. Oxygen vacancy diffusion in alumina: New atomistic simulation methods applied to an old problem. *Acta Materialia* **57** (2009), 4765.
(*35*) A. Heuer et al. On the growth of Al2O3 scales. *Acta Materialia* **61** (2013), 6670.
(*36*) E. Schrödinger. Quantisierung als Eigenwertproblem. *Annalen der Physik* **384** (1926), 361–376.
(*37*) M. Born and R. Oppenheimer. Zur Quantentheorie der Molekeln. *Annalen der Physik* **389** (1927), 457–484.
(*38*) R. V. Noorden, B. Maher, and R. Nuzzo. *The top 100 papers*. 2014. URL: `https://www.nature.com/news/the-top-100-papers-1.16224` (visited on 03/24/2019).
(*39*) P. Hohenberg and W. Kohn. Inhomogeneous Electron Gas. *Physical Review* **135** (1964), B 865.
(*40*) L. H. Thomas. The Theory of Complex Spectra. *Proceedings of the Cambridge Philosophical Society* **23** (1927), 542.

(*41*) E. Fermi. *Rend. Accad. Lincei.* **6** (1927), 602.
(*42*) W. Kohn and L. Sham. Self-Consistent Equations Including Exchange and Correlation Effects. *Physical Review* **140** (1965), A1133–A1138.
(*43*) A. Cohen, P. Mori-Sanchez, and W. Yang. Fractional spins and static correlation error in density functional theory. *Journal of Chemical Physics* **129** (2008), 121104.
(*44*) W. Kohn and L. Sham. One-Particle Properties of an Inhomogeneous Interacting Electron Gas. *Physical Review* **145** (1966), 561–567.
(*45*) J. P. Perdew and Y. Wang. Accurate and simple analytic representation of the electron-gas correlation energy. *Physical Review B* **45** (1992), 13244–13249.
(*46*) J. P. Perdew et al. Atoms, molecules, solids, and surfaces: Applications of the generalized gradient approximation for exchange and correlation. *Physical Review B* **46** (1992), 6671–6687.
(*47*) J. P. Perdew, K. Burke, and M. Ernzerhof. Generalized Gradient Approximation Made Simple. *Physical Review Letters* **77** (1996), 3865–3868.
(*48*) P. Hasnip et al. Density functional theory in the solid state. *Philosophical Transactions of the Royal Society A* **372** (2014), 20130270.
(*49*) V. Fock. Näherungsmethode zur Lösung des quantenmechanischen Mehrkörperproblems. *Zeitschrift für Physik* **61** (1930), 126–148.
(*50*) C. Adamo and V. Barone. Toward reliable density functional methods without adjustable parameters: The PBE0 model. *Journal of Chemical Physics* **110** (1998), 6158–6170.
(*51*) A. Becke. Density-functional thermochemistry. III. The role of exact exchange. *Journal of Chemical Physics* **98** (1993), 5648–5652.
(*52*) B. Himmetoglu et al. Hubbard-Corrected DFT Energy Functionals: The LDA+U Description of Correlated Systems. *International Journal of Quantum Chemistry* **114** (2014), 14.
(*53*) V. Anisimov and O. Gunnarsson. Density-functional calculation of effective Coulomb interactions in metals. *Physical Review B* **43** (1991), 7570.
(*54*) V. Anisimov et al. Density-functional theory and NiO photoemission spectra. *Physical Review B* **48** (1993), 16929.
(*55*) I. Solovyev, P. Dederichs, and V. Anisimov. Corrected atomic limit in the local-density approximation and the electronic structure of d impurities in Rb. *Physical Review B* **50** (1994), 16861.
(*56*) L. Versluis and T. Ziegler. The Determination of Molecular Structures by Density Functional Theory. The Evaluation of Analytical Energy Gradients By Numerical Integration. *Journal of Chemical Physics* **88** (1988), 322–328.
(*57*) J. Andzelm, R. Fournier, and D. Salahub. Analytical gradient of the linear combination of Gaussian-type orbitals-local spin density energy. *Journal of Chemical Physics* **90** (1989), 6371.
(*58*) N. Ashcroft and N. Mermin. *Solid State Physics*. Saunders Collage, 1976.
(*59*) H. Monkhorst and J. Pack. Special points for Brillouin-zone integrations*. *Physical Review B* **13** (1976), 5188.
(*60*) D. Vanderbilt. Soft self-consistent pseudopotentials in a generalized eigenvalue formalism. *Physical Review B* **41** (1990), 7892–7895.